

Modeling of dynamic and post-dynamic recrystallization by coupling a full field approach to phenomenological laws

Ludovic Maire^{a,*}, Benjamin Scholtes^a, Charbel Moussa^a, Nathalie Bozzolo^a, Daniel Pino Muñoz^a, Amico Settefrati^b, Marc Bernacki^a

^a*MINES ParisTech, PSL - Research University, CEMEF - Centre de mise en forme des matériaux, CNRS UMR 7635, CS 10207 rue Claude Daunesse 06904 Sophia Antipolis Cedex, France.*

^b*Transvalor S.A., 694 avenue Maurice Donat, 06250 Mougins, France*

Abstract

This paper describes a level set framework for the *full field* modeling of dynamic and post-dynamic recrystallization in a 3D polycrystalline material with an accurate description of grains topology at large deformation and application to 304L austenitic stainless steel. Topological evolutions are simulated based on a kinetic law linking the velocity of the boundaries to the thermodynamic driving forces. Recrystallization is modeled by coupling a level set approach to phenomenological laws describing strain hardening mechanism and nucleation criteria. Although the proposed formalism does not consider crystal plasticity because of its computational costs, it enables to reach outstanding dynamic recrystallization computations in a front-capturing finite element framework comparatively to the state of art.

Keywords: microstructures, grain boundaries, recrystallization, metallic materials, finite elements, level set.

Funding: This research did not receive any specific grant from funding agencies in the public, commercial, or not-for-profit sectors.

*Corresponding author

Email address: ludovic.maire@mines-paristech.fr (Ludovic Maire)

1. Introduction

Hot deformation of metals is responsible of a wide range of phenomena occurring in the microstructure. At high temperatures, the dislocation density is the result of a competition between the increase of the amount of dislocations due to plastic work and its decrease due to dynamic recovery. In general, the increase is faster than the decrease and the dislocation density globally goes up. Once a critical dislocation density is locally reached, the recrystallization mechanism (i.e. nucleation of recrystallized grains) occurs in the microstructure. These recrystallized grains have a low energy compared to the deformed ones. Because of stored energy gradients between recrystallized and non-recrystallized grains, recrystallized grains grow by consuming deformed grains. Simultaneously, dislocation density increases in the recrystallized grains because of plastic deformation. Capillarity effects (leading to the decrease of the total grain boundaries surface) are also present and play a role regarding the evolution of multiple junctions. All these mechanisms acting during hot deformation lead to the so-called discontinuous dynamic recrystallization process (DDRX) [1, 2, 3, 4] which is the classical dynamic recrystallization (DRX) mechanism for low/medium stacking fault energy (SFE) metallic materials such as the 304L austenitic steel considered for application in this work. If the plastic deformation is stopped and the material is still at high temperature, grain boundary migration is still active because of stored energy gradients and capillarity effects. Furthermore, the nucleation mechanism can still occur in some hardened grains. These mechanisms appearing after hot deformation lead to the so-called post-dynamic recrystallization process (PDRX)[5, 6]. A review of dynamic recrystallization phenomena occurring in metals has been recently proposed in [4].

Since many decades, phenomenological recrystallization models have been proposed like the well-known Avrami relationship aiming to describe the global recrystallized fraction during hot deformation [7, 8, 9]. Many years later, new recrystallization models emerged with the intention to implicitly describe the microstructure by considering spherical grains [10, 11, 12, 13, 14]. In these models, each physical mechanism is described by a physical or phenomenological law. Grains evolve by computing a velocity

between each grain and the averaged microstructure: these kinds of models are often called *mean field* models. The main advantage of these models is related to the fact that they provide good results in terms of recrystallized fraction or mean grain size and they also provide additional information in terms of grain size distribution and dislocation density distribution. However, the topology of grains and the interactions between neighboring grains cannot be described using *mean field* models. Thus several assumptions on the grain mean curvature or on nucleation sites can considerably limit their use.

In parallel, finer approaches called *full field* models have emerged in the last decades. These approaches consider a complete description of the microstructure at the polycrystal scale, which makes the modeling of local phenomena such as abnormal grain growth possible. A review of the most significant numerical methods is given in [15]. Probabilistic voxel-based approaches such as *Monte Carlo* [16, 17] and *cellular automata* [18, 19] are very popular. These models consider uniform grids composed of cells to model microstructure and stochastic laws to predict the motion of interfaces. These simulations are efficient in term of computational cost and the scalability is excellent. On the other hand, deterministic approaches, based on the resolution of partial differential equations, are more accurate in the description of the involved physical mechanisms although they are numerically more expensive. For instance, the *vertex* approach [20] is based on an explicit description of interfaces in terms of vertices. Interfaces motion is imposed at each increment by computing the velocity of a set of points. A major drawback of this approach is related to the complexity of handling all the possible topological events, such as disappearance and appearance of new grains, which is not straightforward especially in 3D. Other deterministic approaches avoid these topological problems since they are based on an implicit description of the interfaces: the *phase-field* [21, 22] and the *level set* (LS) method [23, 24]. The major limitation of these two methods is generally the computational cost but recent improvements of this weakness should be emphasized [22, 25]. LS simulations in context of regular grids and Fourier transform resolution can be found for grain growth [26, 27] and for static recrystallization [25] modeling. When global or local meshing/remeshing operations have to be considered (large deformation, accuracy in the grain interfaces,

presence of second phase particles...), LS approach in context of unstructured finite element (FE) mesh has to be considered [24, 28, 29, 30, 31, 32]. The numerical LS framework developed in [32] is considered and enhanced for DRX modeling in the following.

Several DRX models based on a *full field* approach exist in the literature. In the last decades, [33] has already proposed a 2D model of DRX based on the cellular automata method for interfaces tracking and phenomenological laws to describe hardening and nucleation mechanisms. More recently in [30], a 2D model considering a FE based LS approach is proposed to model DRX. In [34], a coupled crystal plasticity and cellular automata approach has been developed to model DRX in a titanium alloy. In [35], a combined crystal plasticity and vertex model is proposed in 2D to model DRX for large deformation. In [36], a coupled crystal plasticity and cellular automata approach is used in 2D to model DRX in magnesium alloys. In [37], a 3D model based on the phase-field method coupled with a fast Fourier transform based elasto-viscoplastic model is proposed to model DRX in copper. In [38], a 2D cellular automata model has been used to model DRX in Inconel 718 alloy. In [39], a coupled crystal plasticity and cellular automata approach has been proposed in 3D for modeling DRX in titanium alloys. In [40], a 2D cellular automata model coupled to phenomenological laws for strain hardening, recovery and nucleation mechanisms, has been developed to predict microstructural evolutions in a magnesium alloy during hot deformation. In parallel, several analytical models have been recently proposed in order to simulate DRX as a function of the input process conditions [41, 42, 43, 44].

Although literature already provides a large number of papers on *full field* DRX models, a major drawback is the difficulty to handle grains topology and morphology for large deformation (for instance $\epsilon > 0.2$), which is a major limitation since many industrial processes go well further in deformation. Furthermore, crystal plasticity is generally used in *full field* DRX models since it predicts accurately the local evolution of dislocation density at the polycrystal scale. However, the use of crystal plasticity often leads to prohibitive computational costs. Finally, most of DRX *full field* models are developed in 2D because of numerical issues and computational costs. Microstructural

evolutions present a three-dimensional character, therefore results obtained from 2D models may not be representative of a real 3D process. Some limitations of 2D models
95 are related to the location of nuclei, their initial size or growth rates.

In the present work, a 3D-FE model based on the LS method in context of unstructured tetrahedral mesh is proposed to model the DRX and PDRX phenomena with applica-
tion to 304L steel. This model is able to describe grain topology at large deformation
100 (for instance $\epsilon > 2$) with relatively low computational costs. The equations proposed and validated in a *mean field* model [13, 12] are used in this model to simulate the nucleation, work hardening and recovery mechanisms while the LS approach coupled to a remesher provides an accurate tracking of interfaces (i.e. grain boundaries) all along the simulation. The first section of the paper introduces the modeling of the
105 grain boundaries network and grain boundary kinetic. This section is followed by the presentation of the main constitutive equations of the models. Then, a sensitivity study of optimal model parameters (mesh size, initial number of grains, deformation step, time step and critical nucleus radius) on microstructural responses of the model is investigated. The subsequent section presents a comparison between our *full field* model
110 and a *mean field* model of the literature [12] in given thermomechanical conditions.

2. Microstructure and grain boundary migration

2.1. Representation of the initial grain boundaries network and energy field

The model considered in this paper is based on a LS description of the interfaces within a FE framework [24, 29, 30, 15]. First, grain interfaces are virtually generated
115 by using the Voronoï tessellation or Laguerre-Voronoï method [45, 46, 47, 48, 49]. The virtual interfaces are then described into an unstructured FE mesh thanks to LS functions (see appendix A for more details about the generation of the grain boundaries network and appendix B for an introduction of the LS method in the considered polycrystalline framework).

120

A 3D digital microstructure representative of 304L steel has been generated according to a Laguerre-Voronoi algorithm and using the LS approach within a FE framework. The grain size follows a log-normal distribution and result is presented in Fig. 1(a). The mean grain radius $\langle R \rangle$ and the standard deviation σ_R of the distribution are $60\mu\text{m}$ and $10\mu\text{m}$, respectively. The color code corresponds to the equivalent spherical grain radius. The number of grains in the Representative Volume Element (RVE) is around 8000, the number of mesh elements is around 3.5M and 22 LS functions are used.

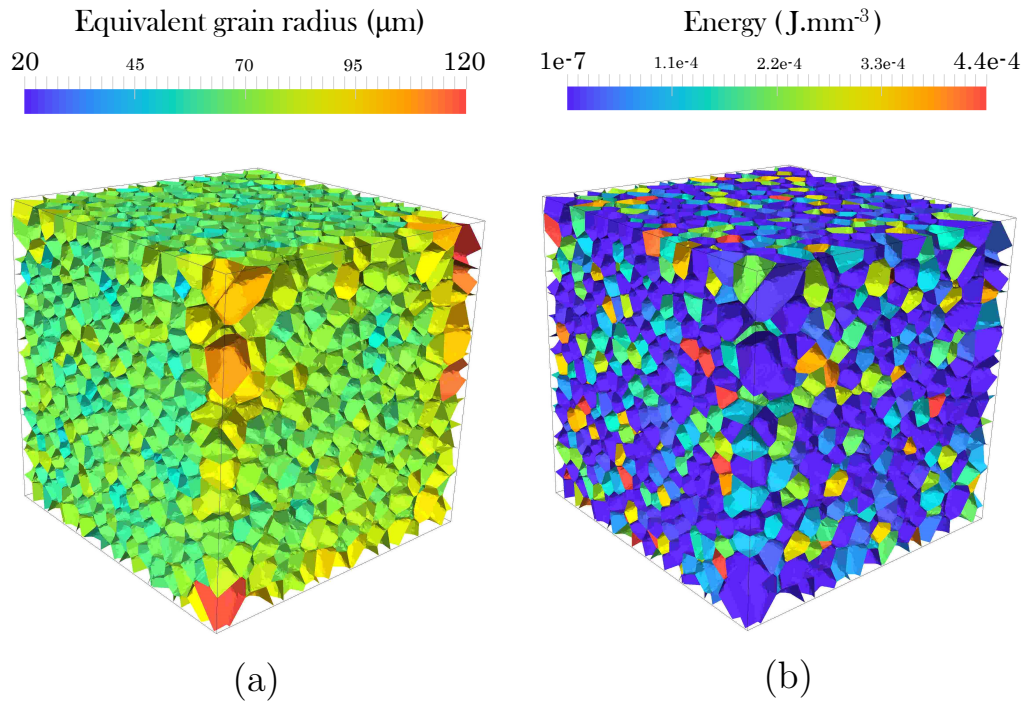


Figure 1: 3D digital microstructure generated according to a Laguerre-Voronoi algorithm following a Log-normal distribution ($\langle R \rangle = 60\mu\text{m}$; $\sigma_R = 10\mu\text{m}$). (a) Color code corresponds to the equivalent spherical grain radius. (b) Color code corresponds to the energy field considered constant per grain and generated from a Gaussian distribution ($\langle E \rangle = 1e-5\text{ J.mm}^{-3}$; $\sigma_E = 2e-4\text{ J.mm}^{-3}$).

At the initial stage of the simulation, an energy field considered constant per grain is defined in the microstructure. This energy field can be generated either according to a particular distribution (Gaussian, log-normal, bimodal) or from experimental data. In the case presented in Fig. 1(b) representative of 304L steel, an initial energy field

is generated from a Gaussian distribution. The mean energy $\langle E \rangle$ and the standard deviation σ_E of the distribution are $1e-5 \text{ J.mm}^{-3}$ and $2e-4 \text{ J.mm}^{-3}$, respectively. An energy field E is related to a dislocation density field ρ and vice versa according to the following relation :

$$E = \tau\rho, \quad (1)$$

where τ represents the dislocation line energy and is considered as material dependent.

2.2. Grain boundary migration

As detailed in the introduction, during a process at high temperature, grain interfaces migrate due to the stored energy gradient across the interface and due to the grain boundary mean curvature which is the sum of the main curvatures in the 3D case. Grain boundary migration is modelled in the considered model by using the strategy adopted in [32]. Since we used the formalism of equations proposed and validated in [13, 12], we also made, although this consideration has not at yet a clear physical sense, the velocity term dependent on the strain rate by considering an additional term $\delta(\dot{\epsilon})$ into the velocity formula (see appendix C for more details concerning the modeling of the grain boundary migration kinetic and about the term $\delta(\dot{\epsilon})$).

3. Dynamic and post-dynamic recrystallization modeling

3.1. Strain hardening and recovery mechanisms

During plastic deformation, dislocations density increases in the microstructure due to strain hardening, resulting in an increase of the stored energy. However, a part of dislocations can also annihilate due to dynamic recovery. The strain hardening and recovery mechanisms appearing during hot deformation, can be modeled at different scales: at a local scale with crystal plasticity [35, 36, 50] or at a macroscopic scale with phenomenological laws [51, 52, 53]. In this model, phenomenological laws are considered to limit the computational cost of the 3D simulations, thus none resolution of a mechanical problems is considered. The deformation is simply modeled by applying a normal velocity on different faces of the RVE so as to respect a given strain rate

and a velocity gradient. Each mesh node is thus displaced according to these velocities. During deformation, the faces of the RVE remain plane (homogeneous material
160 assumption) and the volume conservation of the RVE is ensured (incompressible material).

Considering N_G grains in the microstructure, the averaged dislocation density field obtained from Eq. 1 in each grain j noted $\langle \rho_j \rangle$, is assumed to evolve according to the
165 Yoshie-Laasraoui-Jonas law [53] :

$$\frac{\partial \langle \rho_j \rangle}{\partial \varepsilon_{\text{eff}}^p} = K_1 - K_2 \langle \rho_j \rangle, \quad (2)$$

where $\varepsilon_{\text{eff}}^p$ denotes the effective plastic strain, K_1 and K_2 are two constants which represent the strain hardening and dynamic recovery term, respectively. At each time increment, this differential equation is solved with an Euler explicit method, i.e. :

$$\frac{\langle \rho_j \rangle^{(t+\Delta t)} - \langle \rho_j \rangle^t}{\Delta \varepsilon} = K_1 - K_2 \langle \rho_j \rangle^t, \quad (3)$$

where $\Delta \varepsilon$ is equal to $\dot{\varepsilon}_{\text{eff}}^p \times \Delta t$ with Δt the time step, which leads to the final equation :

$$\langle \rho_j \rangle^{(t+\Delta t)} = K_1 \Delta \varepsilon + (1 - K_2 \Delta \varepsilon) \langle \rho_j \rangle^t. \quad (4)$$

170 When a grain boundary migrates, the swept area is almost free of defects, i.e. dislocations-free. This phenomenon is traduced by a decrease of the dislocation density in growing grains. Thus a minimal dislocation density ρ_0 , which is material dependant, is attributed to swept areas. Then the new dislocation density is averaged in each grain following the equation :

$$\langle \rho_j \rangle^{(t+\Delta t)} V^{(t+\Delta t)} = \langle \rho_j \rangle^t V^t + \Delta V \rho_0, \quad (5)$$

175 where ΔV represents the swept volume between the instants t and $(t + \Delta t)$. Fig. 2 shows the evolution of a dislocation density field in a grain between t and $(t + \Delta t)$ due to strain hardening, dynamic recovery and grain boundary migration mechanisms.

— Grain boundary at t
 ---- Grain boundary at $t + \Delta t$

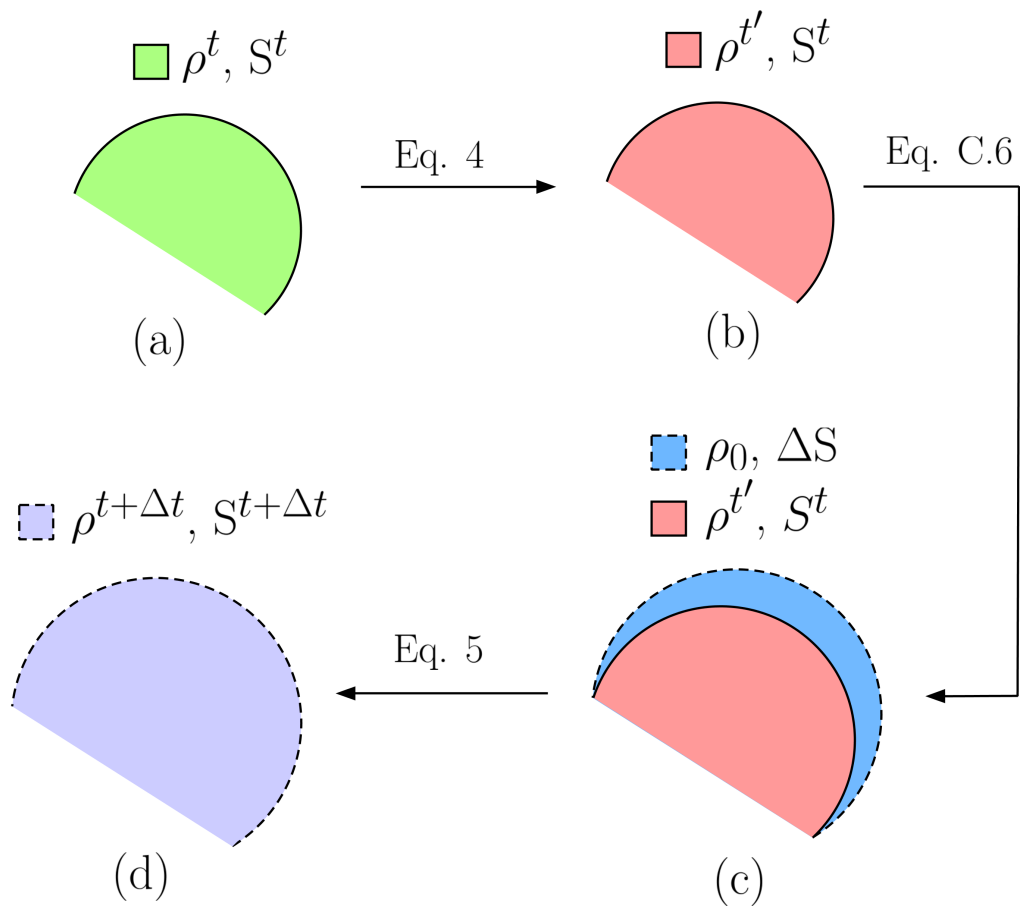


Figure 2: 2D scheme illustrating the evolution of a dislocation density field of a single grain due to the mechanisms of strain hardening and dynamic recovery⁹(from (a) to (b)), grain boundary migration(from (b) to (c)) and decrease of dislocation density due to boundary migration(from (c) to (d)) between the instants t and $(t + \Delta t)$ of the simulation.

The PDRX mechanism is taken into account after deformation by modeling the migration of grain boundaries (see section 2.2.), the decrease of dislocation density due to boundary migration given by Eq. 5 and the static recovery due to annihilation of dislocations given by Eq. 6 :

$$\langle \dot{\rho}_j \rangle = -K_s \langle \rho_j \rangle, \quad (6)$$

where K_s is a temperature dependant parameter which represents the static recovery term and a superposed dot denotes differentiation with respect to time. During PDRX, no nucleation of recrystallized grains is considered, thus the following section on nucleation only concerns DRX mechanism.

The mean flow stress σ_j in the j^{th} grain is computed during deformation from its average dislocation density $\langle \rho_j \rangle$ using the Taylor equation :

$$\sigma_j = \sigma_0 + \alpha \mu b \sqrt{\langle \rho_j \rangle}, \quad (7)$$

where σ_0 is a dislocations-free yield stress and α is a constant. Then the total flow stress $\langle \sigma \rangle$ is calculated as a volume average of the flow stresses in all grains :

$$\langle \sigma \rangle = \frac{\sum \sigma_j V_j}{V_{\text{tot}}}. \quad (8)$$

3.2. Nucleation mechanism

When enough energy is accumulated in the material due to plastic deformation, some dislocation networks can develop within grains and tend to form new recrystallized grains called nuclei, mainly located at grain boundaries [54]. Different criteria need to be verified locally in order to obtain a substructure that becomes a nucleus: a mobile high-angle grain boundary has to be formed by the nucleation event, a high stored energy gradient across the interface must be present in order to provide enough positive driving pressure for counter the capillarity effects applied on the nucleus. In the considered framework, as γ_b is assumed isotropic, only the stored energy and the critical nucleus radius is taken into account for nucleation event.

3.2.1. Nuclei location

The adopted strategy concerning the creation of new nuclei in a FE-LS framework is based on the recent developments of Scholtes et al. [32]. In the considered model, we assume that new nuclei of critical radius r^* only appear close to grain boundaries. This restriction is taken into account by forcing the centers of new nuclei inside a layer $\pm L$ around the interfaces, where $L = r^*$ (see Fig. 3 for more details).

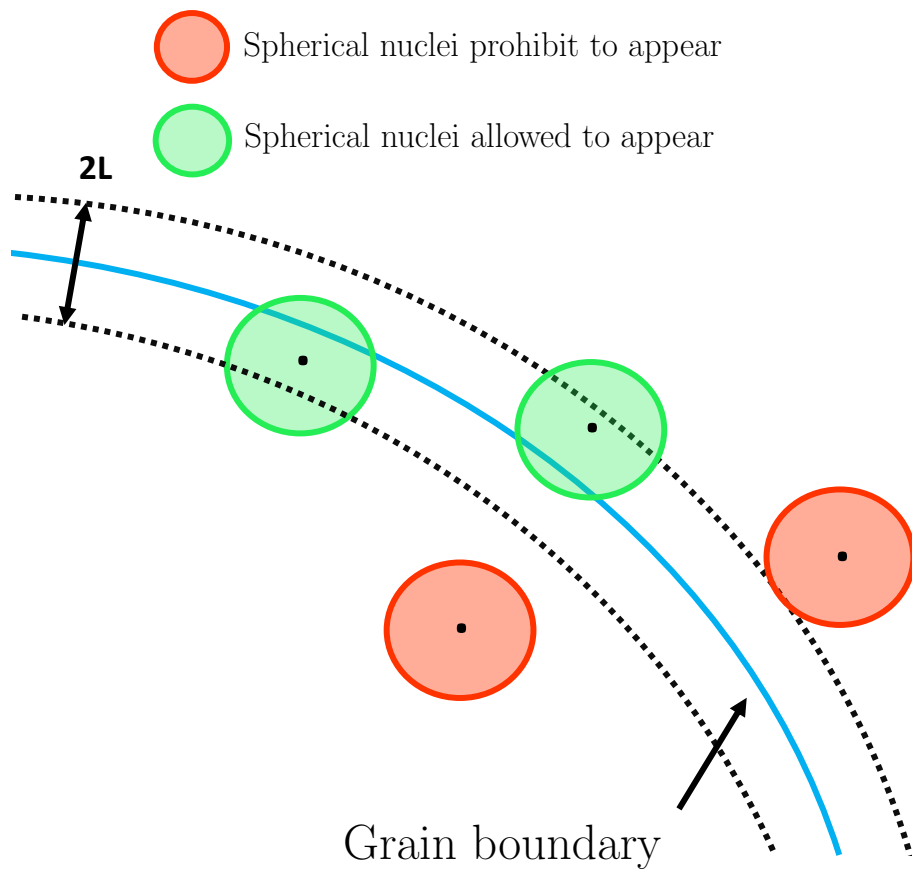


Figure 3: Examples of nuclei that are allowed (green color) and prohibit (red color) to appear depending on the distance from the grain boundary to their centers.

3.2.2. Critical stored energy for nucleation

In the considered model, we assume that a new nucleus can appear if the averaged stored energy in its appearance area reaches a critical value ρ_{cr} (see Fig. 4). This restriction is taken into account by averaging the energy in the volume occupied by the nucleus before its appearance, and by verifying if this averaged energy reaches ρ_{cr} . (see Fig. 4 for more details). If this condition is verified and if its position satisfies the condition presented previously, the new nucleus can be created with a stored energy ρ_0 .

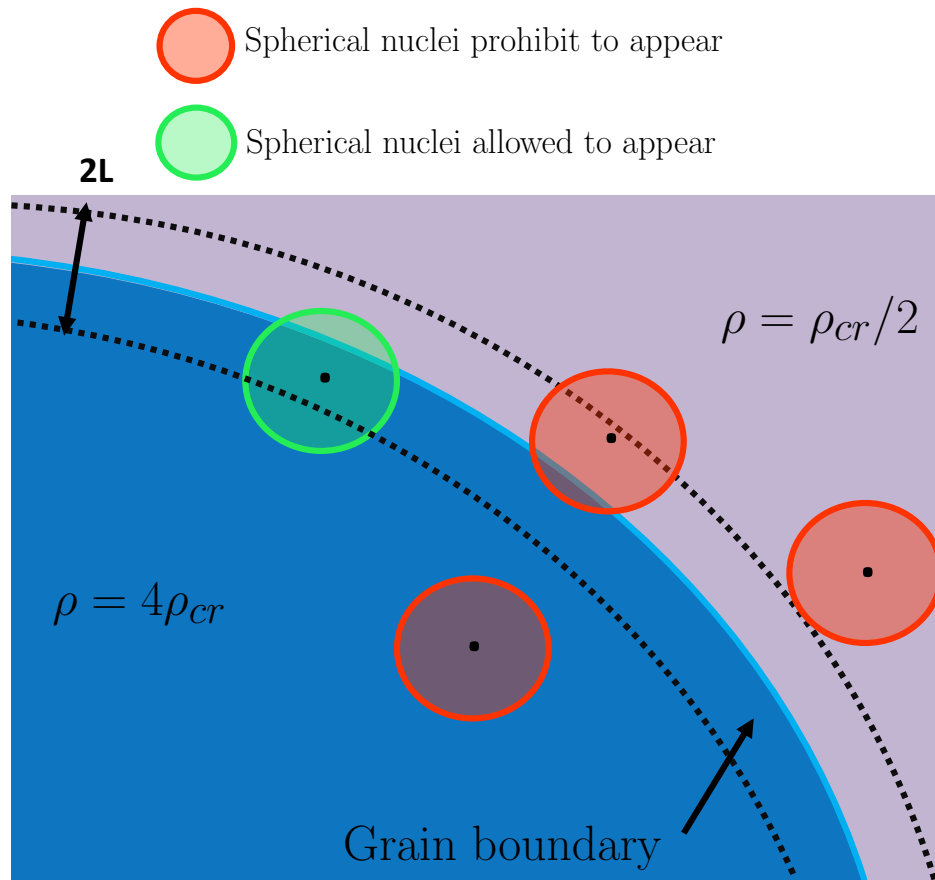


Figure 4: Examples of nuclei allowed (green) and prohibit (red) to appear depending on whether the averaged stored energy in the volume occupied by each nucleus before its appearance reached the critical dislocation density ρ_{cr} .

215 Concerning the computing of ρ_{cr} , a first approximation is made and an iterative calculation of ρ_{cr} is done according to the following equation [13] :

$$\rho_{\text{cr}} = \left[\frac{-2\gamma_{\text{b}}\dot{\epsilon} \frac{K_2}{M_{\text{b}}\delta(\dot{\epsilon})\tau^2}}{\ln\left(1 - \frac{K_2}{K_1}\rho_{\text{cr}}\right)} \right]^{1/2}, \quad (9)$$

where M_{b} is the grain boundary mobility and γ_{b} is the grain boundary energy.

220 The influence of the temperature on ρ_{cr} is taken into account in Eq. 9 thanks to the parameters K_2 and M_{b} while the influence of the strain rate on ρ_{cr} is taken into account in Eq. 9 thanks to the parameters K_1 , K_2 , $\dot{\epsilon}$ and $\delta(\dot{\epsilon})$. It is assumed that ρ_{cr} increases when decreasing temperature or increasing strain rate.

225 3.2.3. Nucleus critical radius

When a new nucleus appears in the microstructure, its critical radius must be high enough so that its stored energy counters the capillarity forces applied by the neighboring grains. This corresponds to the condition when the stored energy of the material is large enough to overcome the capillarity effects exerted by neighboring grains on the nucleus. This condition is approximated by the so-called Bailey-Hirsch criterion [55] :

$$r^* = \omega \frac{2\gamma_{\text{b}}}{\rho_{\text{cr}}\tau}, \quad (10)$$

where $\omega > 1$ is a safety factor ensuring that the created nucleus has a required driving force for growth. Indeed the Eq. 10 with $\omega = 1$ is based on the assumption that a new nucleus is perfectly spherical but in the present model, depending on the mesh size, the nucleus cannot be perfectly spherical, which justifies the use of the safety factor ω .

235 The value of ω will be investigated in the section 4.

3.2.4. Nucleation rate

The nucleation rate \dot{V} representing a volume of nuclei per unit of time, is calculated according to a variant of the proportional nucleation model of Peczak and Luton [56] :

$$\dot{V} = K_g \Phi \Delta t, \quad (11)$$

where $K_g(T, \dot{\epsilon})$ is a probability coefficient related to the thermo-mechanical conditions,
240 i.e. the temperature and the effective plastic strain rate and Φ represents the total
boundary area (in a necklace-type nucleation) or total volume (in a bulk-type nucle-
245 ation) of grains verifying $\rho_i > \rho_{cr}$.

For better understanding of the coupling between LS method and recrystallization gov-
245 erning laws, a flow chart summarizing the resolution method of the present model for
a given process time is presented in Fig. 5.

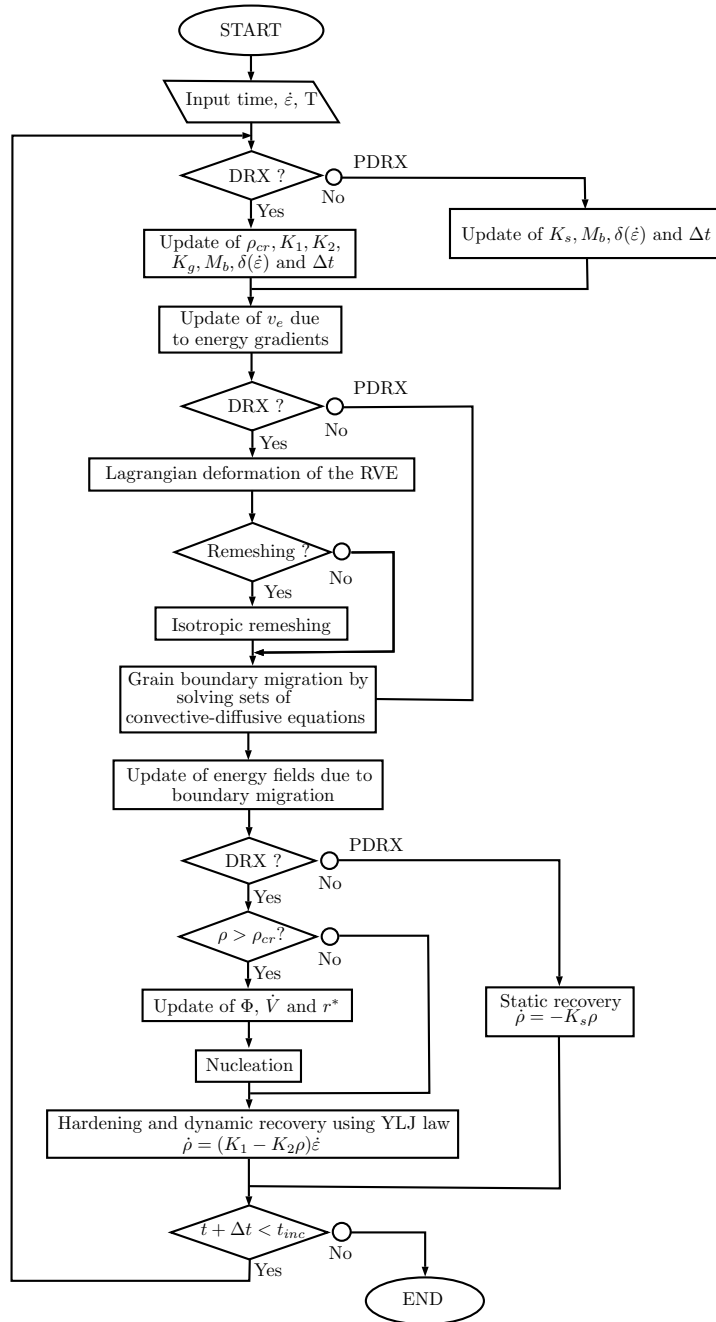


Figure 5: Scheme describing the resolution method of the present model for a given process time, strain rate $\dot{\epsilon}$ and temperature T .

4. Sensitivity study of the present model

The DRX and PDRX model considered many parameters which have to be correctly initialized in order to model as accurately as possible the microstructural mechanisms, while keeping relatively low computational costs. This section is dedicated to a sensitivity study of initial parameters leading to converged results of DRX (see 4.1.) and then PDRX (see 4.2.).

4.1. Dynamic recrystallization

An identification of the optimal mesh size, initial number of grains, deformation step and critical nucleus radius of the DRX model leading to converged results while keeping low computational costs is done in this section.

Mesh size

A single nucleus is considered and the mesh size is calibrated so as to obtain a good description of this nucleus in terms of surface and volume. The isotropic mesh size must be small enough to correctly describe the nucleus mean curvature but also reasonable in order to limit the computational cost. Thus four spherical nuclei of radius $20\mu\text{m}$ are generated using four different mesh sizes and results are presented in Fig. 6. The quantity ξ corresponds to the ratio between the nucleus radius r^* and the mesh size and is reported below each nucleus in Fig. 6. The quantity E_v corresponds to the L^1 error between the volume of the generated nucleus of radius r^* (presented in Fig. 6) and the volume of a sphere of radius r^* . The error between the surfaces is also measured and noted E_s . These values are reported below each nucleus in Fig. 6.

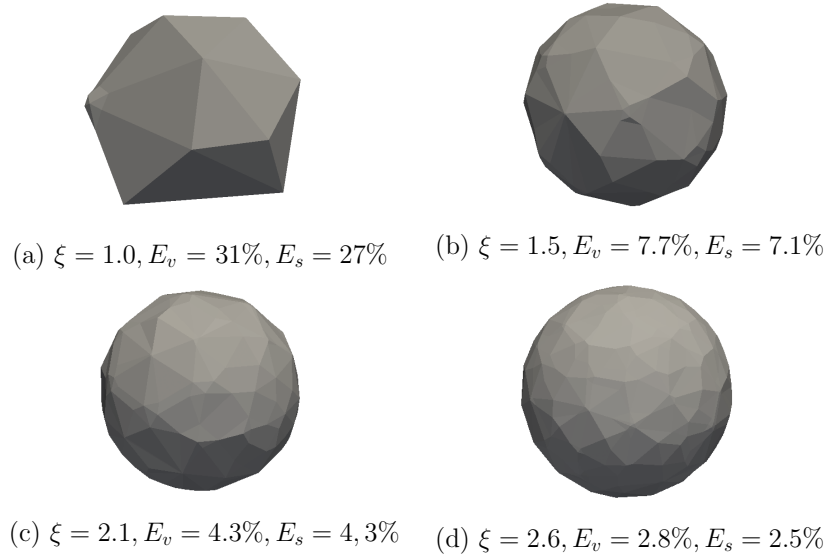


Figure 6: Four nuclei generated according to different mesh sizes. ξ corresponds to the ratio between the nucleus radius r^* and the mesh size. E_v (resp. E_s) corresponds to the L^1 error between the volume (resp. surface) of the generated nucleus and the volume (resp. surface) of a sphere of same radius.

It is observed that in each case, the E_v error is close to the E_s error. The nucleus presented in Fig. 6(a) has large E_v and E_s errors (31% and 27%, respectively). The three other nuclei presented in Fig. 6(b), (c) and (d) give E_v and E_s errors lower than 10%, leading to a better description of the nuclei in these three cases. A ratio $\xi \simeq 2$ between the nucleus radius and the mesh size is chosen as a good compromise between a minimum number of mesh elements into the nucleus and low E_v and E_s errors. Thus, the future number of mesh elements in the simulations will always be chosen so as to respect a ratio $\xi \simeq 2$.

Initial number of grains

Several *full field* simulations of DRX have been performed using the considered model for a temperature of 1273°K and a strain rate of $0.01s^{-1}$ during 300s. The deformation of the RVE is idealized at each increment by updating all mesh nodes coordinates at

the instant $t + \Delta t$ thanks to the relations :

$$\begin{aligned}x^{t+\Delta t} &= x^t, \\y^{t+\Delta t} &= (1 + \dot{\epsilon}\Delta t)y^t, \\z^{t+\Delta t} &= (1 - \dot{\epsilon}\Delta t)z^t,\end{aligned}\tag{12}$$

with $(x^t; y^t; z^t)$ and $(x^{t+\Delta t}; y^{t+\Delta t}; z^{t+\Delta t})$ the coordinates of a mesh node at the instants t and $t + \Delta t$ respectively, considering the $(0, \vec{x}, \vec{y}, \vec{z})$ Cartesian coordinate system (see Fig. 7), $\dot{\epsilon}$ the strain rate following the direction of solicitation (i.e. direction \vec{z}) and Δt the time increment. These equations lead to an idealized channel-die case, where the six faces remain plane during the simulated process. Computations were performed on three nodes of 24 CPU processors each in order to compare computational costs. The variation of the initial number of grains is done by keeping the same initial mean grain radius ($\simeq 60\mu\text{m}$) and by varying the RVE size (from 0.14mm^3 to 0.34mm^3). The safety factor ω (Eq. 10) is taken equal to 2, leading to a critical nucleus radius of $7\mu\text{m}$. The mesh size is fixed to $3\mu\text{m}$ in order to validate the ratio $\xi \simeq 2$. The step deformation is taken low enough (2%) to ensure a good convergence of calculations. Microstructures are presented in Fig. 7 and results in terms of recrystallized fraction, mean grain radius, mean dislocation density, computational cost, grain radius distribution and dislocation density distribution are plotted in Fig. 8. The mean grain radius $\langle R_{\text{vol}} \rangle$ and the mean dislocation density $\langle \rho_{\text{vol}} \rangle$ are weighted by grain volume. The distributions are plotted for a true deformation $\epsilon = 1$. Only grains from 0 to $12\mu\text{m}$ have been considered in Fig. 8(e) since these grains represent more than 99% of the total number of grains in the microstructure. It is clearly observed that a total of 8 grains in the initial microstructure leads to results as close as with a number of 20 or 40 grains (see Fig. 8). Indeed our nucleation model considers a random nucleation on high energy grain boundaries. So during the DRX mechanism when all grains have a sufficient energy, nuclei will appear everywhere at every interfaces and the total number of grains rapidly increases in the microstructure, reducing the influence of the initial number of grains in this case. Two simulations with two different initial number of grains (8 and 27 grains) and exactly the same initial grain radius distribution and energy distribution are presented in Fig. 7.

It is clearly observed for a deformation $\varepsilon = 1.5$ that the volumic fractions of nuclei are similar in the two cases. Thus it is assumed that the accuracy of the results is sufficient
310 with an initial number of 8 grains.

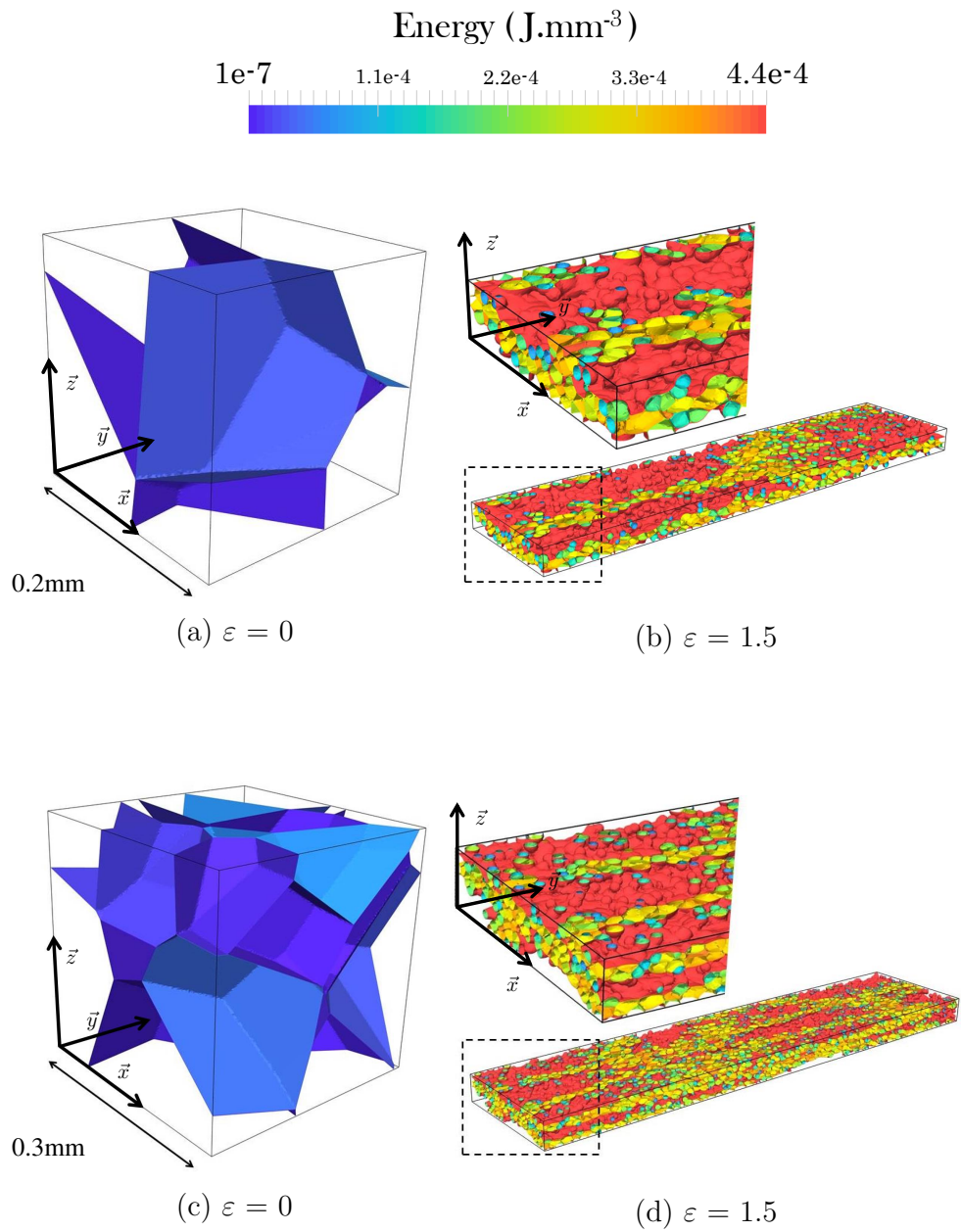


Figure 7: Two simulations using two different initial number of grains : 8 initial grains for a true deformation $\varepsilon = 0$ (a) and $\varepsilon = 1.5$ (b). 27 initial grains for a true deformation $\varepsilon = 0$ (c) and $\varepsilon = 1.5$ (d). The simulated process is a channel-die configuration at 1273°K and a strain rate of 0.01s^{-1} during 150s.

Furthermore, using 8 initial grains instead of 40 initial grains reduces the computational cost by a factor of 9, which is a non negligible time saving (see Fig. 8(d)). An initial number of 3 grains has also been tested. However, this small number of grains lead
315 to artefacts (important influence of the boundary conditions, a too small number of grains to respect precisely the input grain size distribution and an insufficient total grain boundary surface for the appearance of new grains after few time increments) and therefore to non-physical results, in particular concerning the distributions (see Fig. 8(e) and (f)). Thus, a minimum initial number of 8 grains will be chosen for all
320 the future simulations.

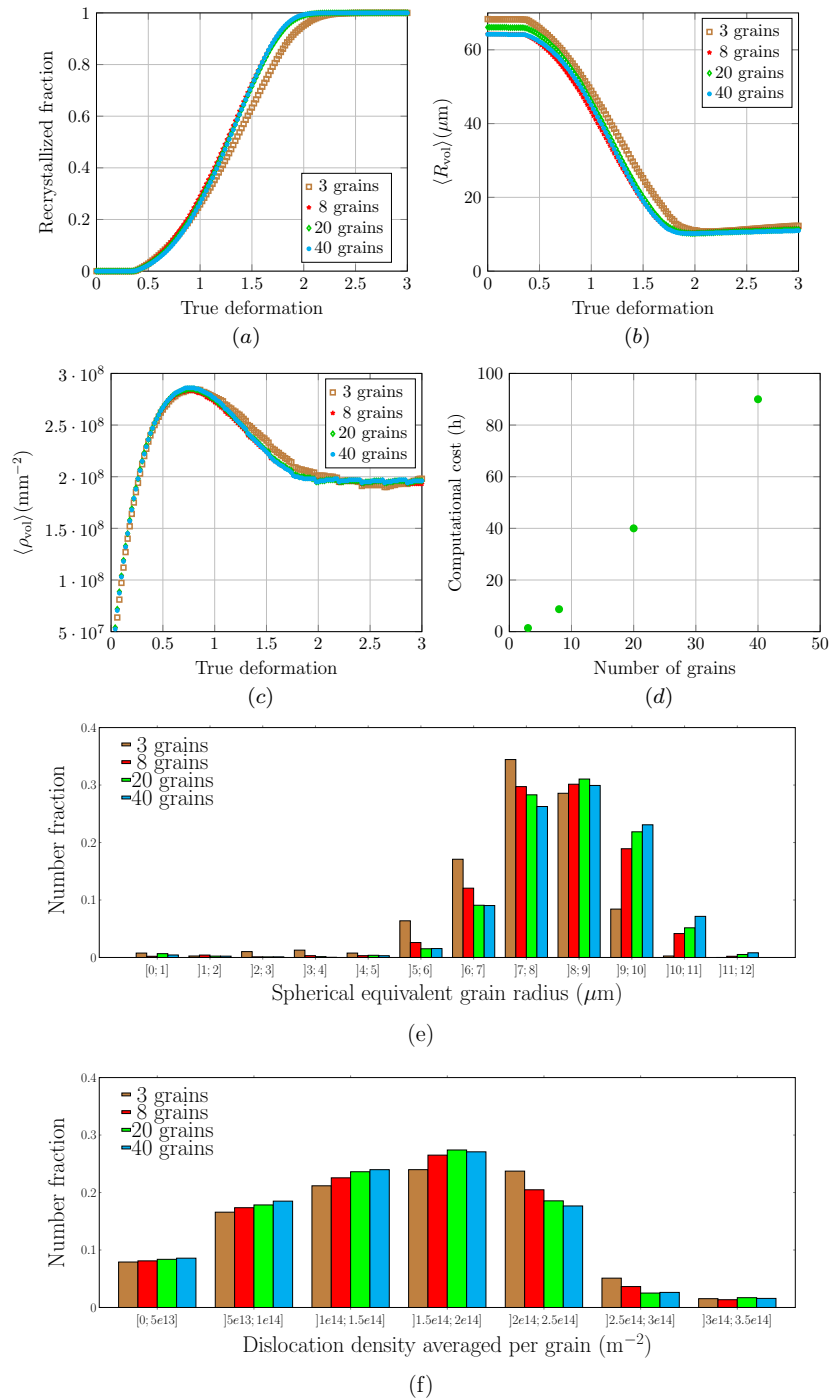


Figure 8: Sensitivity of the initial number of grains on polycrystal results: (a) recrystallized fraction, (b) mean grain radius, (c) mean dislocation density, (d) computational cost, (e) grain radius distributions for a true deformation $\epsilon = 1$ and (f) dislocation density distributions for a true deformation $\epsilon = 1$. The simulated process is a channel-die compression at 1273°K, at a strain rate of 0.01s^{-1} during 300s. The mean values are weighted by grain volume for a better representativeness of the curves at the onset of recrystallization.

Deformation step

The strain hardening and recovery laws are directly related to the deformation step (see Eq.2). Therefore a fixed time step is not enough to ensure convergence for any strain rate since the deformation step is given by the product between the time step and the strain rate. Thus, the idea of this section is to look for a deformation step that leads to converged results and then to use this ideal deformation step to deduce the associated time step.

According to the previous study, the initial number of grains is now fixed to 8 grains. The safety factor ω and the mesh size are still fixed and equal to 2 and $3\mu\text{m}$, respectively. To investigate the optimal deformation step, several simulations were done for four deformation steps (2%;5%;10%;20%). The same results as the previous section (i.e. recrystallized fraction, mean grain radius, mean dislocation density, computational cost, grain radius distribution and dislocation density distribution) have been investigated in Fig. 9. When the deformation step decreases, results (recrystallized fraction, mean dislocation density, mean grain radius, grain radius distribution and dislocation density distribution) converge toward the same trends. The computational cost is reduced by a factor of about 2 between 2% and 5% of deformation step while keeping close results (see computational cost in Fig. 9(d)). Thus a deformation step of 5% is chosen as a good compromise for all the future simulations.

Critical nucleus radius

The initial number of grains and deformation step are fixed to 8 and 5% respectively, and the influence of the critical nucleus radius, more particularly the safety factor noted ω and used in Eq. 10, is thereafter investigated. Four different values for ω are tested (1;1.5;2;3) leading to the use of four different mesh sizes in order to respect the ratio $\xi \simeq 2$. The same results as the previous section (i.e. recrystallized fraction, mean grain radius, mean dislocation density, computational cost, grain radius distribution and dislocation density distribution) have been investigated in Fig. 10. First, it is observed that the final mean grain radius $\langle R_{\text{vol}} \rangle$ and the grain radius distribution are highly influenced by the critical nucleus radius r^* . This observation is important because it means that the final mean grain radius can be directly influenced by the safety factor ω . By

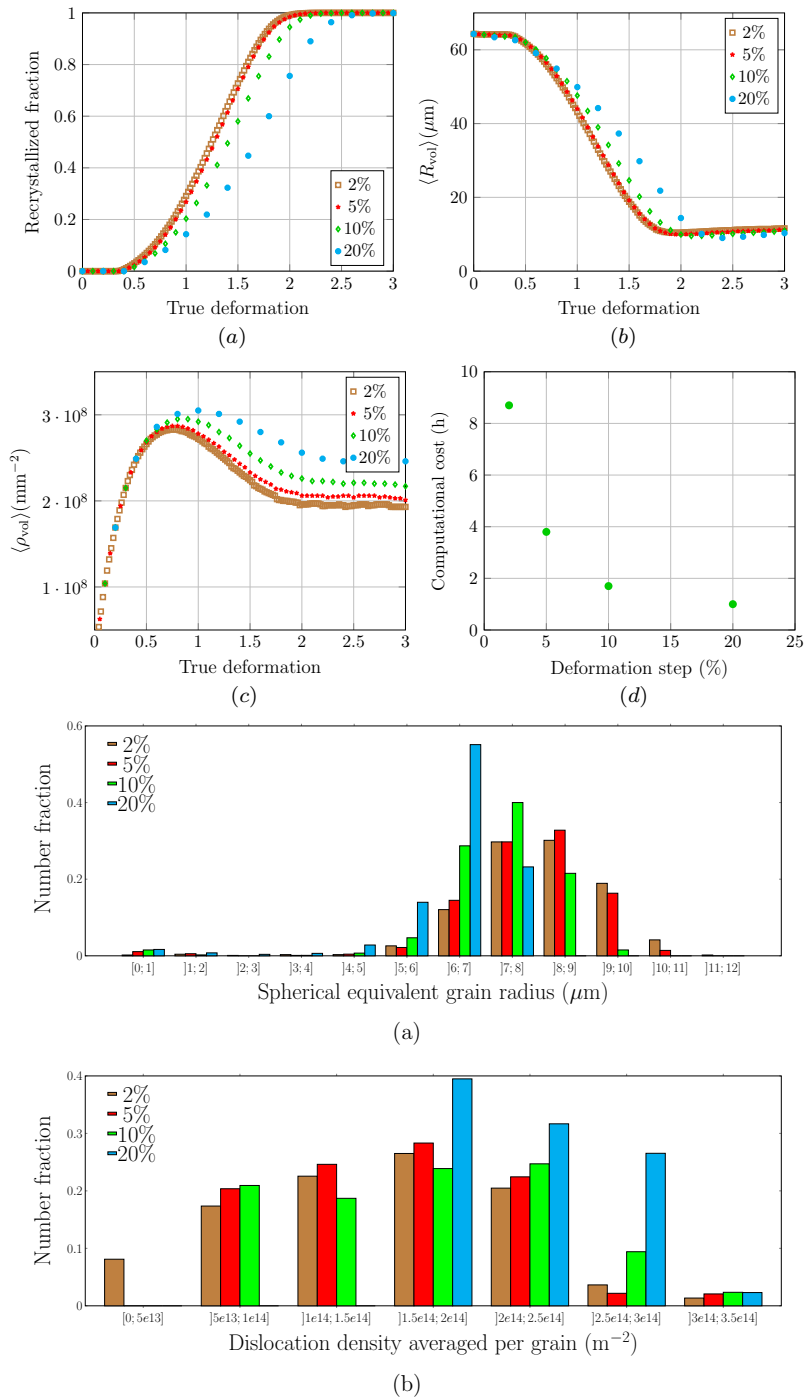


Figure 9: Sensitivity of the deformation step on polycrystal results: (a) recrystallized fraction, (b) mean grain radius, (c) mean dislocation density, (d) computational cost, (e) grain radius distributions for a true deformation $\epsilon = 1$ and (f) dislocation density distributions for a true deformation $\epsilon = 1$. The simulated process is a channel-die compression at 1273°K, at a strain rate of 0.01s^{-1} during 300s. The mean values are weighted by grain volume for a better representativeness of the curves at the onset of recrystallization.

observing the four other curves, it is clearly observed that a safety factor of 1 does not lead to converged results. This is due to the fact that a safety factor of 1 leads to a critical nucleus radius too low to counter capillarity effects exerted by neighboring
355 grains and thus the new nuclei do not survive, which explains the observed kinetic of recrystallized fraction. In contrast, the two safety factors of 1.5 and 2 lead to a good convergence of all presented results. Finally, a safety factor of 3 does not lead to converged results in terms of recrystallized fraction and mean dislocation density because the critical nucleus radius is too large using this value and therefore results predicted by
360 the model might be non-physical. Thus a safety factor of 1.5 is chosen as the optimal value for the future simulations.

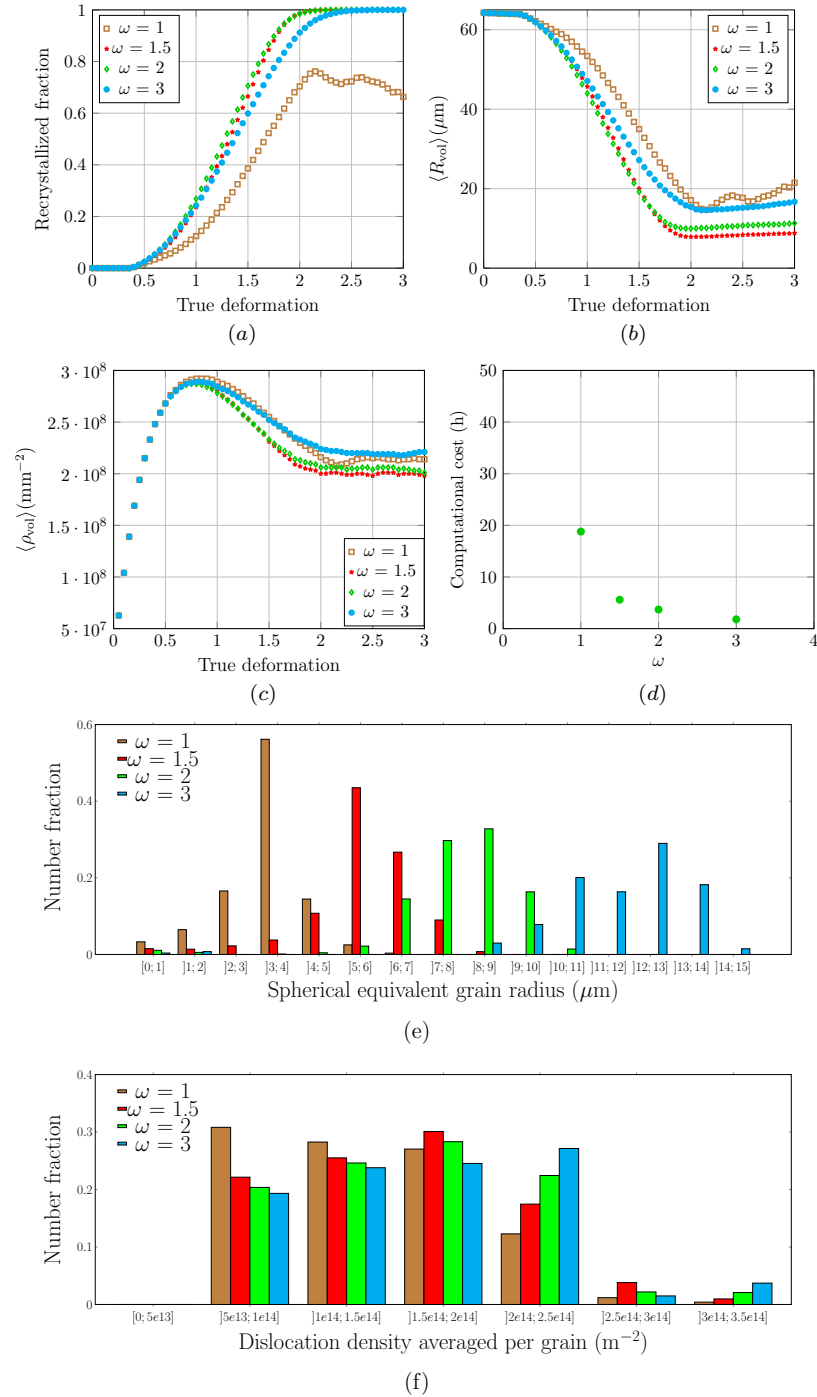


Figure 10: Sensitivity of the critical nucleus radius on polycrystal results: (a) recrystallized fraction, (b) mean grain radius, (c) mean dislocation density, (d) computational cost, (e) grain radius distributions for a true deformation $\epsilon = 1$ and (f) dislocation density distributions for a true deformation $\epsilon = 1$. The simulated process is a channel-die compression at 1273°K, at a strain rate of 0.01s^{-1} during 300s. The mean values are weighted by grain volume for a better representativeness of the curves at the onset of recrystallization.

4.2. Post-dynamic recrystallization

Time step

The second convergence study concerns the ideal time step (Δt) used for PDRX simulations. If the displacement of a grain boundary is too high during Δt , the kinetic cannot be correctly captured. Thus, a solution is to adapt Δt as a function of a maximum displacement of grain boundaries. Let's consider the maximum displacement of an interface d_{\max} in a microstructure between t and $(t + \Delta t)$. This latter is given by the maximum velocity v_{\max} in the microstructure between these two instants times the time increment Δt :

$$d_{\max} = v_{\max} \times \Delta t. \quad (13)$$

Furthermore, the highest value for v_{\max} is reached if the smallest possible grain having the highest possible mean energy is surrounded by the largest possible grain having the lowest possible mean energy. Thus by using classical approximations for grain mean curvature, v_{\max} is estimated as follow :

$$v_{\max} \simeq M_b \left(\frac{2\gamma_b}{\langle R \rangle} + \Delta E \right), \quad (14)$$

where $\Delta E = E_{\max} - E_{\min}$. In context of anisotropy of M_b and/or γ_b , the same methodology could be used by using in Eq.14 the maximum values of these physical parameters. Finally by combining Eqs. 13 and 14, the max displacement d_{\max} is estimated at each step time by :

$$d_{\max} \simeq M_b \left(\frac{2\gamma_b}{\langle R \rangle} + \Delta E \right) \times \Delta t. \quad (15)$$

Then, it is necessary to find the ideal maximum displacement of grain boundaries in order to determine the time step Δt at each increment thanks to Eq. 15. In this study, we choose to defined the ideal maximum displacement d_{\max} as a percentage of mesh size and this choice is validated in the following.

4.2.1. Validation of the criterion for time step

385 To be representative of the PDRX mechanism, we assume four different simulations each representing a nucleus growing in a matrix (see Fig. 11). Each simulation is related to particular thermomechanical conditions (i.e. a couple of °K and $\dot{\epsilon}$) leading to a given critical nucleus radius r^* (by using Eq. 10) and leading to a maximum dislocation density field in the matrix computed by the ratio K_1/K_2 which is the steady state dislocation density according to Eq. 2 (since K_1 and K_2 depend on °K and $\dot{\epsilon}$).
 390 Furthermore, a dislocation density field $\rho_0 = 1e11 \text{ m}^{-2}$, which is material dependant, is defined into the nucleus. We note R_p the ratio between the stored gradient energy (ΔE) and the capillarity effect ($2\gamma_b/r^*$). For each case, the mesh size is chosen so as to keep the ratio ξ between the nucleus radius and the mesh size approximatively equal
 395 to 2 as demonstrated in the DRX sensitivity study of the previous section.

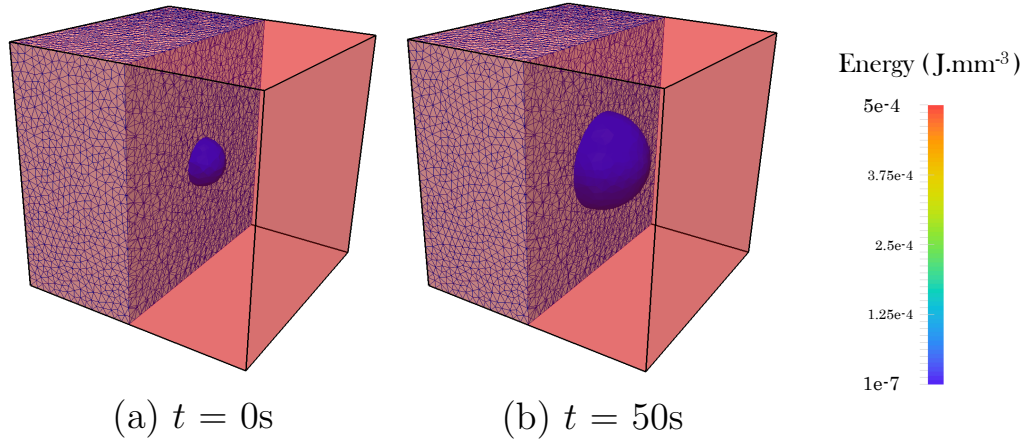


Figure 11: Growth of a nucleus immersed in a matrix. The critical nucleus radius is equal to $5.2 \mu\text{m}$. The energy in the nucleus and in the matrix are $1.47e-7 \text{ J}\cdot\text{mm}^{-3}$ and $4.9e-4 \text{ J}\cdot\text{mm}^{-3}$, respectively.

Different percentages of mesh size from 10% to 40% are investigated as maximum displacement d_{max} . In every cases, the evolution of the nucleus radius obtained by the numerical simulations is confronted to the analytical solution presented below :

$$r^{(t+\Delta t)} = r^t + M_b \Delta t \left(\Delta E - \frac{2\gamma_b}{r^t} \right), \quad (16)$$

The L^2 errors between the analytical solution and the numerical results are plotted in

400 Fig. 12 for each case corresponding to a particular couple of thermomechanical conditions.

First, it is observed in Fig. 12 that the lowest errors are obtained for cases where the gradient stored energy term is dominant (i.e. highest values of R_p). This observation is logical and can be easily explained. The stored energy gradient term computed in the simulation is exact whereas the nucleus mean curvature is estimated by the Laplacian of the distance function and thus is mesh size dependant. Furthermore, as the mesh size is actually isotropic and non-refined around the interface, a non-negligible error can appear on the capillarity term in the simulation. Thus when the stored energy gradient is preponderant compared to the capillarity effects (i.e. high values of R_p), the error made on the estimation of the mean curvature is of second order in the velocity term and lower errors are observed with respect to the analytical solution.

Furthermore for a given nucleus size, the errors are observed dependant on the percentages of mesh size displacement (see Fig. 12). It is observed that the minimum errors are globally obtained for the mesh size displacements of 10%, 20% or 30%. For a very small displacement, the error due to the transport equation resolution of the LS method (see section 2.2.) can be relatively high compared to the small displacement of the interface, which can globally leads to inaccurate results. This aspect can explain that the 10%-case is globally less accurate than the 20%-case. For a large displacement (i.e. 40% of mesh size), the value of displacement seems too high during a single step time and thus the kinetic cannot be correctly captured. Indeed, our FE methodology remains of first order in time and important displacement during one time step can lead to non-physical results. Finally, 10%, 20% or 30% of mesh sizes give better results than 40% of mesh size. However, for reasons of computational costs, we will retain a maximum displacement of mesh size d_{\max} equal to 30% for the future PDRX simulations.

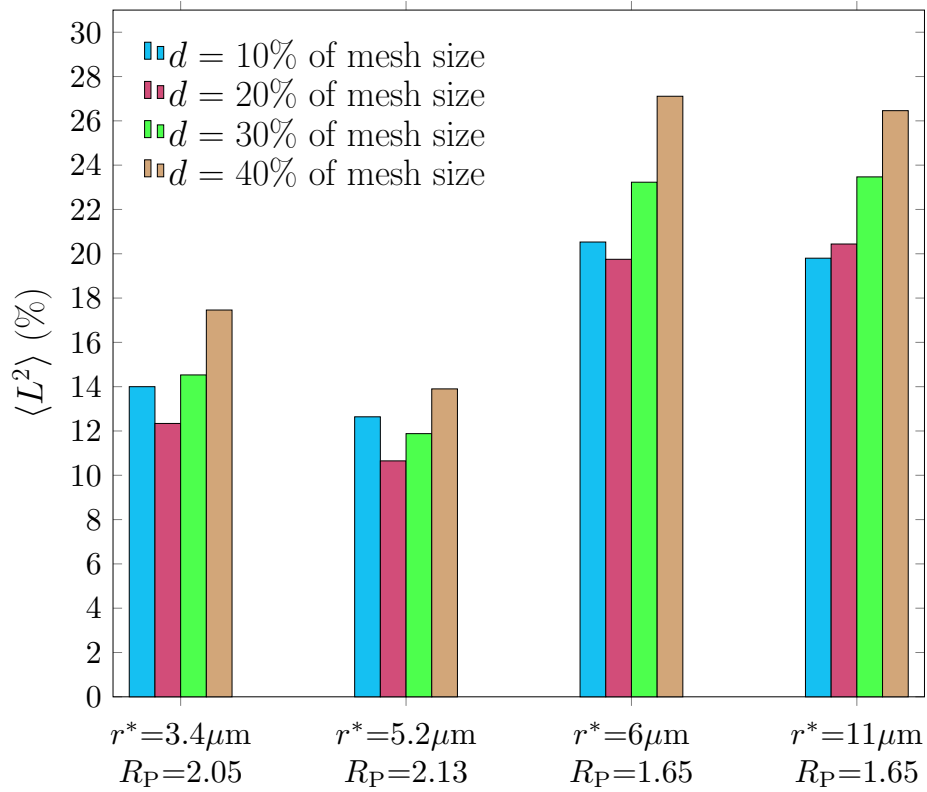


Figure 12: L^2 Error on the equivalent mean grain radius evolution between the *full field* simulation and the scheme defined by Eq. 16. r^* is the critical nucleus radius. R_p is the ratio between the velocity due to capillarity effects and the velocity due to the stored energy gradient. Each color corresponds to a specific displacement of mesh size performed at each increment of the model.

5. Results and comparisons with a *mean field* model

5.1. Dynamic recrystallization

This paper proposes a numerical framework based on phenomenological laws from an existing *mean field* model [13, 12] for nucleation criteria, hardening and recovery. However, contrary to *mean field* models, this model presents the advantage to fully describe, in time and space, the grain boundary network thanks to the level set approach for the modeling of grain boundary motion. Therefore, the idea of this section is to compare the above-mentioned *mean field* model of the literature [13, 12] with

435 this *full field* model in order to observe the influence of respecting the topology of the microstructure. The considered *mean field* model [12, 13] is based on a discrete representation of the microstructure composed of classes of spherical grains having a radius R_i , an averaged dislocation density $\langle \rho_i \rangle$ and a number of grains. The classes are also separated into non-recrystallized and recrystallized classes.

440 The governing laws of hardening, recovery and nucleation mechanisms are identical in the two considered *mean field* and *full field* models. The main limitation of the *mean field* model remains in the grain topology and the direct interactions between grains which is approximated while being explicitly considered in the *full field* model. Thus, we assume that the *full field* model is more accurate than the *mean field* model
 445 in the following comparisons.

The thermomechanical conditions considered in the two models are a hot deformation of a 304L steel at 1273°K and under a strain rate of $0.01s^{-1}$. The duration process is 300s in order to achieve a steady-state regime. In the same manner as previous
 450 simulations, a channel-die compression test is considered in the following *full field* simulation. The set of parameters used in the governing laws of the two models as well as the characteristics of the initial microstructures are representative of the considered 304L steel and are summarized in Tabs. 1 and 2, respectively [13, 57]. A number of 8 initial classes is considered in the *mean field* model since this low number of initial
 455 classes has shown same results as a large number of initial classes. The characteristics R_i and $\langle \rho_i \rangle$ of these 8 classes are identical to the characteristics of the 8 initial grains considered in the *full field* simulation. The number of grains N_i in each class of the *mean field* model is chosen in order to respect the input distribution.

	K_1	K_2	K_g	K_s	M_0	$\delta(\dot{\epsilon})$	γ_b	τ	Q_m
Unity	m^{-2}		m/s	s^{-1}	$m^4/(J.s)$		J/m^2	J/m	J/mol
Values	1.1e15	3.3	3.28e-8	0.001	1.56e-1	1.07	0.6	1.47e-9	2.8e5

Table 1: Set of parameters used in governing laws of both *mean field* and *full field* models for the considered 304L steel [13, 57]. The deformation conditions associated to these parameters are the following : T = 1273°K; $\dot{\epsilon} = 0.01s^{-1}$.

	$\langle R \rangle$	σ_R	$\langle \rho_v \rangle$	σ_ρ
Unity	μm	μm	m^{-2}	m^{-2}
Values	60	10	6.5e13	1.25e13

Table 2: Characteristics of the initial microstructure generated by the Voronoï tessellation algorithm and the associated energy field constant per grain generated from a Gaussian distribution.

The *full field* simulation was performed on 3 nodes of 24 CPU processors. Four differ-
460 ent instants of the *full field* simulation are presented in Fig. 13 with a color code corre-
sponding to the energy field constant per grain. The initial RVE measures 0.2mm^3 and
is composed of 8 grains at the early stage of the simulation while around 9000 grains
are present in the RVE at the end of the simulation.

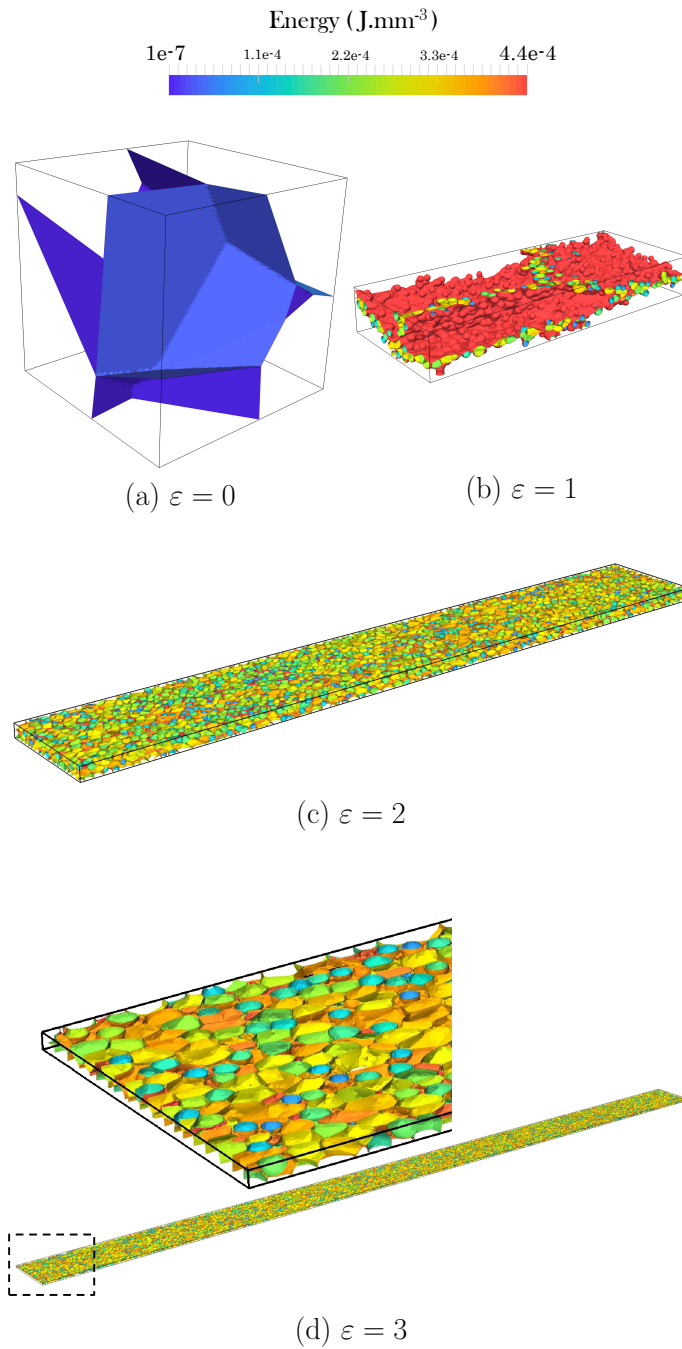


Figure 13: Four instants of a DRX simulation using the present *full field* model. The simulated process is a channel-die compression at 1273°K at a strain rate of 0.01s^{-1} during 300s. Initial microstructure is composed of 8 grains while around 9000 grains are present at the end of deformation. Color code corresponds to the energy field constant per grain.

465 Homogenized results in terms of mean dislocation density $\langle \rho_{\text{vol}} \rangle$, mean grain radius
 $\langle R \rangle$, mean grain radius weighted by grain volume $\langle R_{\text{vol}} \rangle$ and recrystallized fraction are
 confronted between the two models in Fig. 14. First it is observed that the evolutions
 of the mean grain radius $\langle R \rangle$ predicted by the two models are similar during all the
 process duration (see Fig. 14(c)) and final values are slightly higher than the critical
 470 nucleus radius ($r^* = 5.2 \mu\text{m}$). The decrease of $\langle R \rangle$ at the onset of recrystallization ($\varepsilon \simeq$
 0.4) is very fast and thus difficult to capture (see Fig. 14(c)), thus the mean grain radius
 weighted by volume $\langle R_{\text{vol}} \rangle$ is also plotted in Fig. 14(d). During the first minutes of
 process (up to $\varepsilon = 1$), the recrystallized fraction, $\langle R_{\text{vol}} \rangle$ and $\langle \rho_{\text{vol}} \rangle$ evolutions are quasi
 similar between the two models (see Fig. 14(a), (b), (d)). However, for a true deforma-
 475 tion $\varepsilon > 1$, the kinetics are always faster for the *full field* results, meaning that the
 number of nuclei appearing in the microstructure is always larger in the *full field* case.
 A first cause explaining this difference can be the evolution of grain boundary surfaces
 from equiaxed to ellipsoidal shape, increasing the surface of grain boundaries and con-
 sequently increasing the nucleation rate in the *full field* case (Eq. 11). Another cause
 480 explaining this difference is the quantity γ_{RX} presented in Fig. 14(f) and investigated
 in the following.

The quantities called γ_{NR} and γ_{RX} (see [12] for more information about the calcu-
 lation of these quantities) represent respectively the mobile surface fraction of non-
 485 recrystallized grains in contact with recrystallized grains and vice versa. These two
 quantities are used in the *mean field* model in order to calculate the grow rates of re-
 crystallized and non-recrystallized grains. These quantities can be estimated from the
full field simulation and compared with those computed in the *mean field* model. To
 estimate these quantities in the *full field* simulation, the surface fraction of each non-
 490 recrystallized grain in contact with a recrystallized grain is calculated and averaged to
 get the quantity γ_{NR} and vice versa for γ_{RX} . These values are measured at each instant
 of the *full field* simulation and are compared to the *mean field* model in Fig. 14(e) and
 (f). First, the increase of γ_{NR} observed in Fig. 14(e) is quiet similar for the two models.
 Furthermore, this evolution is very fast from the moment where nuclei appear ($\varepsilon \simeq 0.4$).
 495 This fast increase is logical since nucleus mainly appear at grain boundaries, thus most

of non-recrystallized grains are in contact with RX grains as soon as nucleation starts. The decrease of γ_{RX} observed in Fig. 14(f) is perfectly similar for the two models up to a true deformation $\varepsilon \simeq 0.9$. After this instant, the decrease of γ_{RX} is much faster in the *mean field* model. The quantity γ_{RX} is used in the *mean field* model to calculate the growth rate of nuclei, thus a faster decrease of γ_{RX} in the *mean field* case is a cause of the slower evolution of the recrystallized fraction, $\langle \rho_{vol} \rangle$ and $\langle R_{vol} \rangle$ predicted by the *mean field* model (see Fig. 14(a), (b) and (d)).

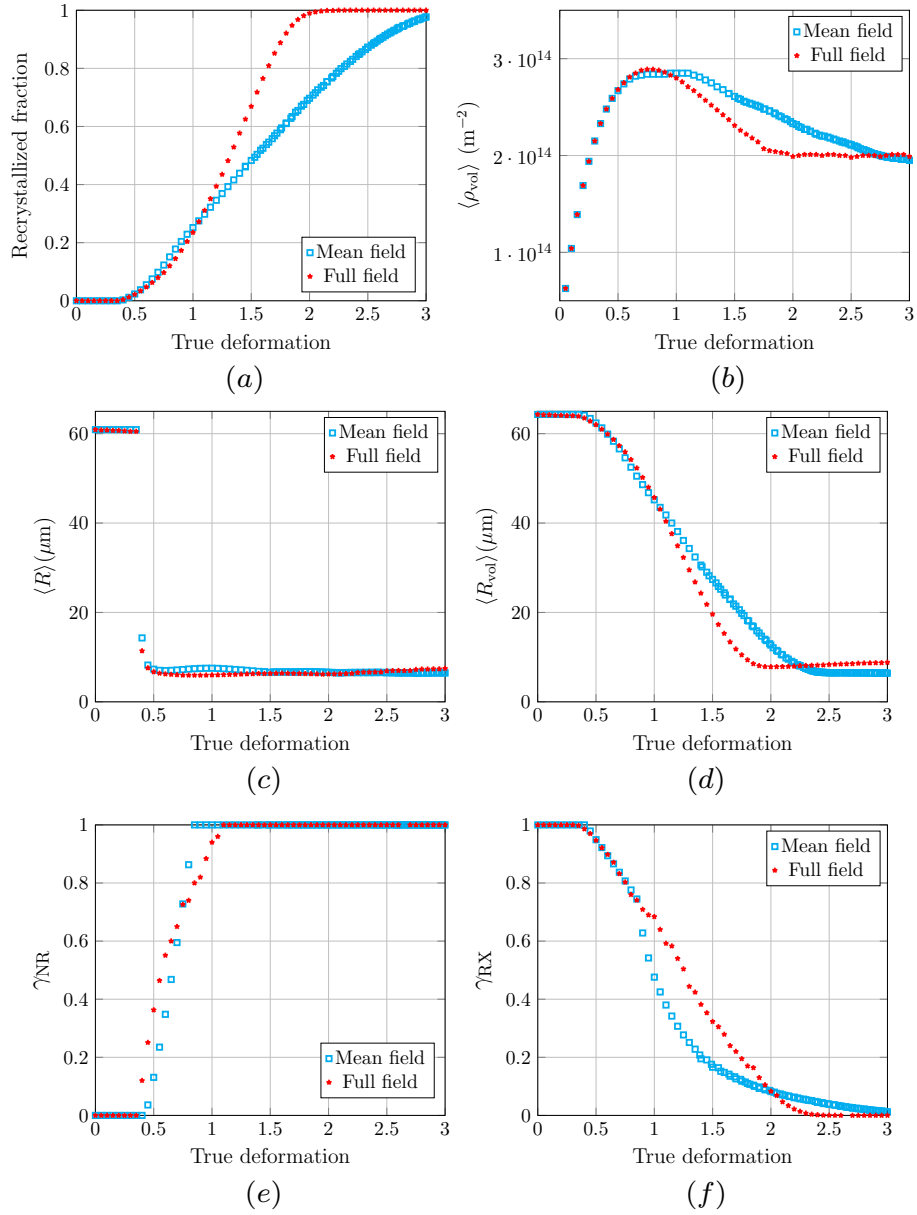


Figure 14: Comparisons of the macroscopic results obtained during a DRX process using the present *full field* model and a *mean field* model of the literature [12]. Compared results are: (a) recrystallized fraction weighted per grain volume, (b) mean dislocation density weighted by grain volume, (c) mean grain size, (d) mean grain size weighted by grain volume, (e) averaged surface fraction of non-recrystallized grains in contact with recrystallized grains and (d) averaged surface fraction of recrystallized grains in contact with non-recrystallized grains. The simulated process is a channel-die compression at 1273°K, at a strain rate of 0.01s^{-1} during 300s.

Grain radius distributions and dislocation density distributions are also compared between the two models at four instants of the simulations (see Fig. 15 and Fig. 16). The grain radius distributions are represented in volume fraction since after few seconds of deformation, the number of nuclei is much higher than the number of initial grains. Thus a number fraction is not a discerning method to follow at the same time the small and large grains. The class width of histograms is $3\mu\text{m}$ for the grain radius distributions and $5e13\text{m}^{-2}$ for the dislocation density distributions.

510

The grain radius distributions predicted by the two models have still some similarities for a true deformation $\varepsilon = 1$ (see Fig. 15(b)). However, for a true deformation $\varepsilon = 2$, a volume fraction of large grains is observed in the *mean field* simulation whereas in the *full field* simulation, the microstructure is fully recrystallized and these large grains have disappeared (see. Fig. 15(c) and (d)). This difference is still due to the quantity γ_{RX} which decreases faster in the *mean field* case, leading to the fact that nuclei slowly growth at the expense of the non-recrystallized grains than in the *full field* case. Finally, a single narrow peak is observed in the *mean field* simulation for a true deformation $\varepsilon = 3$ at the steady-state regime whereas a larger peak is observed in the *full field* simulation (see Fig. 15(d)).

520

Concerning the dislocation density distributions, the shapes of the curves are close for the three instants $\varepsilon = 1$, $\varepsilon = 2$ and $\varepsilon = 3$ of process (see Fig. 16(b), (c) and (d)). At each of these instants, the curves of the *full field* simulation have a more pronounced peak than in the *mean field* simulation.

525

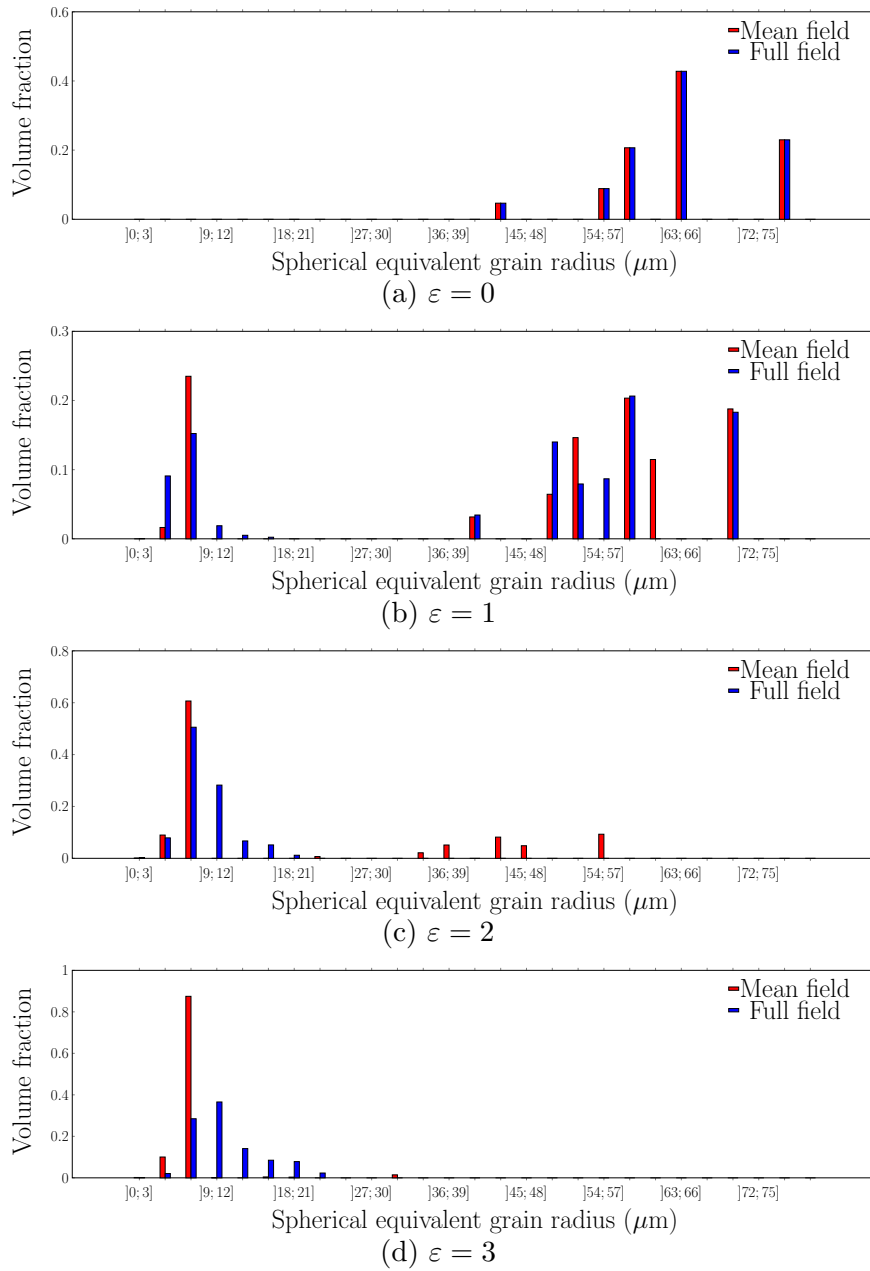
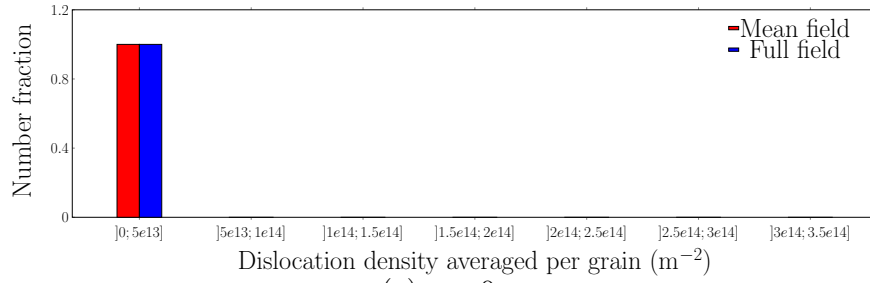
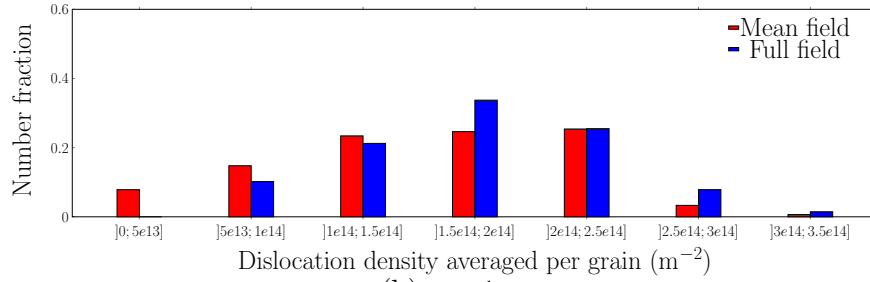


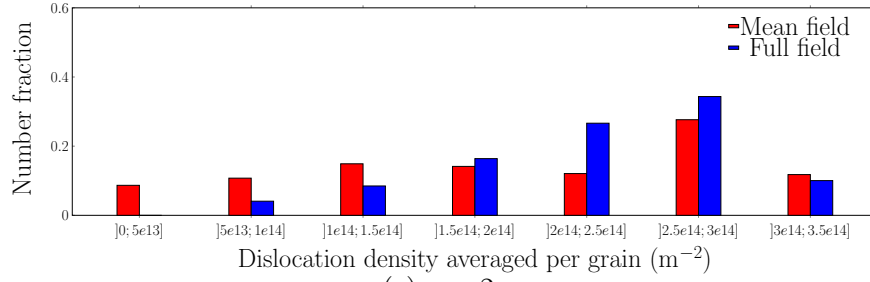
Figure 15: Comparisons, at different instants, of the grain radius distributions ((a) to (d)) obtained during a DRX process using the present *full field* model and a *mean field* model of the literature [12]. The simulated process is a channel-die compression at 1273°K, at a strain rate of 0.01s^{-1} during 300s.



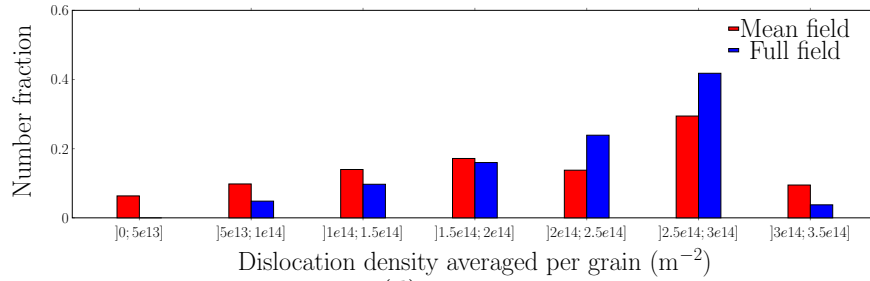
(a) $\varepsilon = 0$



(b) $\varepsilon = 1$



(c) $\varepsilon = 2$



(d) $\varepsilon = 3$

Figure 16: Comparisons, at different instants, of the dislocation density distributions ((a) to (d)) obtained during a DRX process using the present *full field* model and a *mean field* model of the literature [12]. The simulated process is a channel-die compression at 1273°K, at a strain rate of 0.01s^{-1} during 300s.

5.2. Post-dynamic recrystallization

A PDRX simulation is then considered using the two models in order to compare the results. To avoid accumulating differences from DRX, the initial state of the microstructure used in both models corresponds to the final state microstructure obtained after a DRX simulation using the present *full field* model (see the subsection 5.1.). The PDRX process is simulated by considering a 304L steel maintained at 1273°K during 25min. The first two minutes of PDRX are presented in Fig. 17. It is observed a large decrease of energy in the material during the first minutes of PDRX. After these few minutes, the preponderant mechanism is the capillarity driven grain growth mechanism since the energy is low in the material and thus only the mean curvature of grains plays a primordial role on the pressure acting in the grain interfaces.

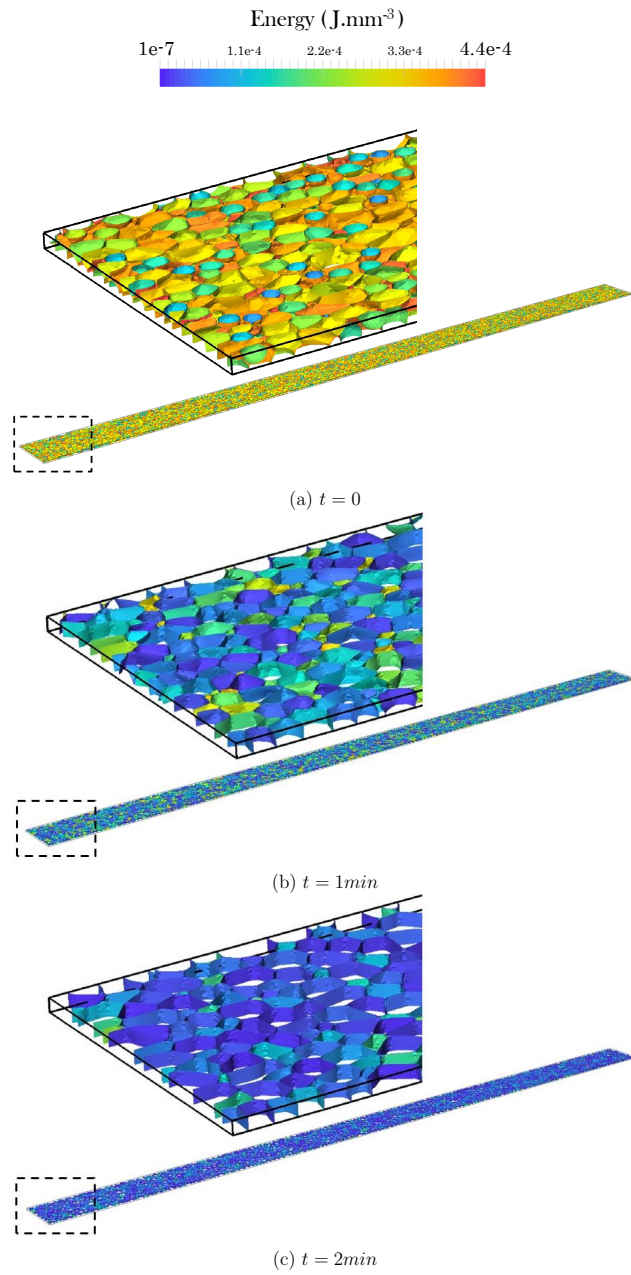


Figure 17: Three instants of the PDRX simulation using the present *full field* model. The simulated process is a heat treatment at 1273°K during 25min. Initial microstructure is composed of 9000 grains while around 600 grains are present at the end of the heat treatment. Color code corresponds to the mean energy per grain.

540 Comparisons of mean dislocation density $\langle \rho_{\text{vol}} \rangle$, mean grain radius $\langle R \rangle$ and mean grain radius weighted by grain volume $\langle R_{\text{vol}} \rangle$ between the two models are presented in Fig. 18. The results obtained according to the two models are close. The evolutions of the curves are very pronounced at the early stage of the simulation since the energy is still high in the material. After few minutes, the energy is much more low in the material (see Fig. 17) and thus the grain boundary kinetic slows down, which is characterized by a slow evolution of $\langle R \rangle$ and $\langle R_{\text{vol}} \rangle$ after this instant in Fig. 18(b) and (c).

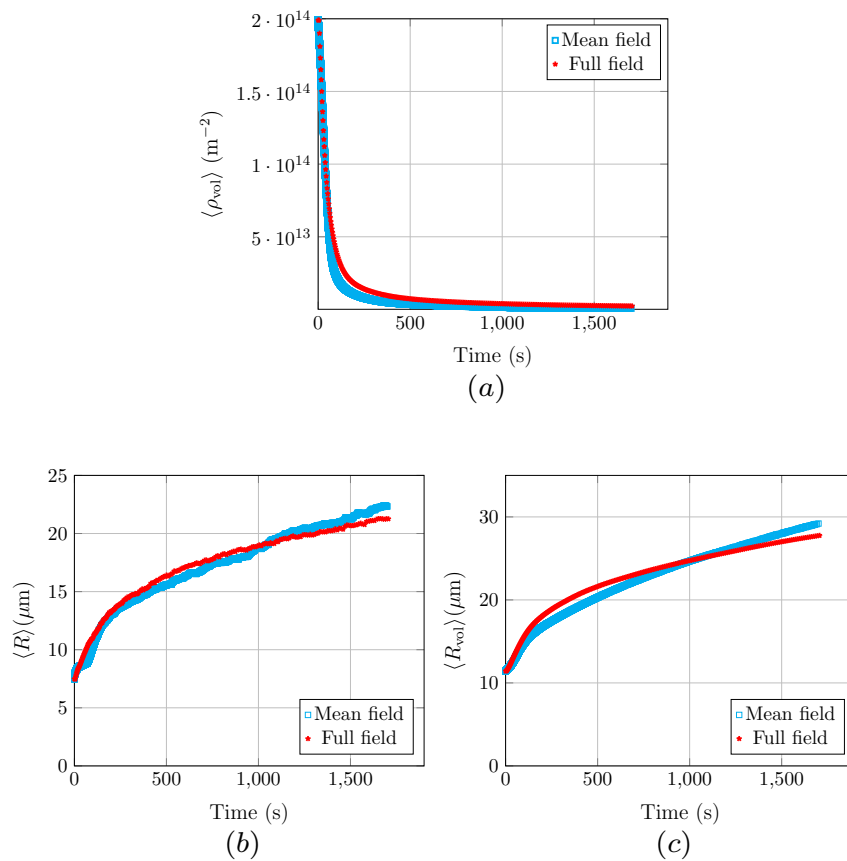


Figure 18: Comparisons of the macroscopic results obtained during a PDRX simulation using the present *full field* model and a *mean field* model of the literature [12]. Compared results are: (a) mean dislocation density weighted by grain volume, (b) mean grain size and (c) mean grain size weighted by grain volume. The simulated process is a heat treatment at 1273°K during 25min.

545 The grain radius distributions and dislocation density distributions are also presented
and compared in Figs. 19 and 20. After 10 min of PDRX, the grain radius distribution
is still very close between the two simulations (see Fig. 19(b)). However, after 20 min
of PDRX, a single higher peak is appearing on the grain radius distribution of the *mean*
field simulation (see Fig. 19(c)) and this peak is still observed after 25min of PDRX
550 (see Fig. 19(d)). In the *full field* simulation, this single higher peak is not observed
during the simulation. Globally, it is observed that the grain radius distribution is poorly
described by the *mean field* model. Concerning the dislocation density distributions,
the results are identical in the two simulations since the energy quickly decreases in the
material and thus after 10min of PDRX, all the grains have the same low energy and a
555 single narrow peak is observed in the two models (see Fig. 20).

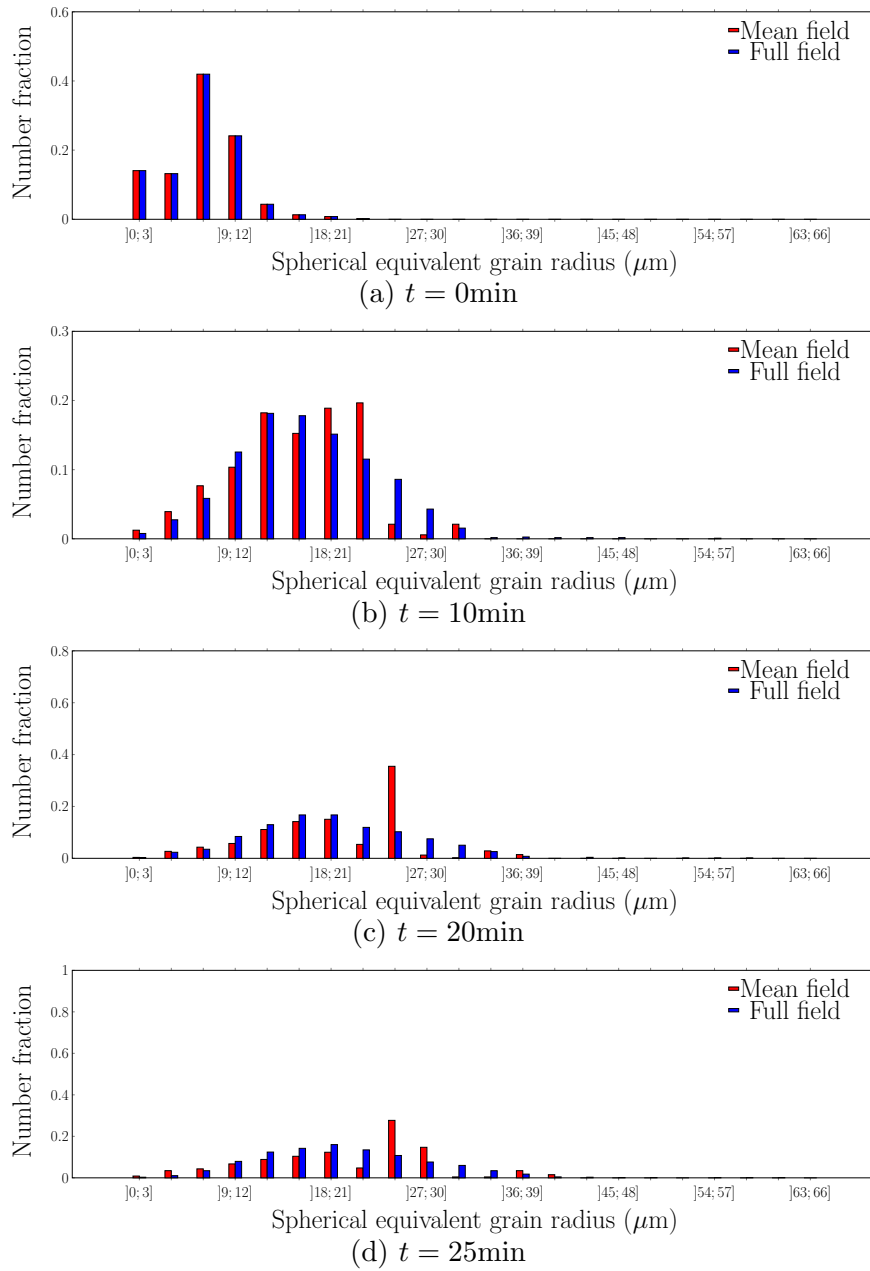
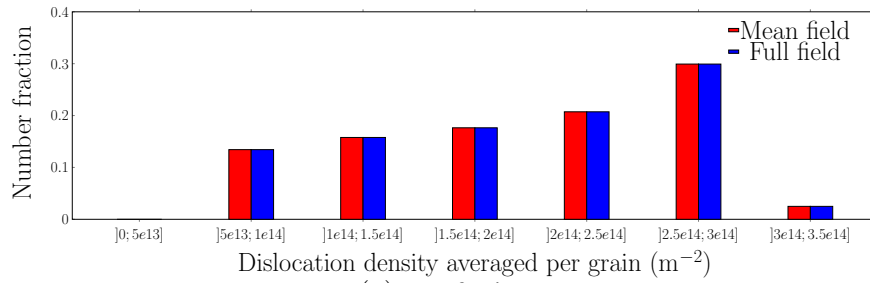
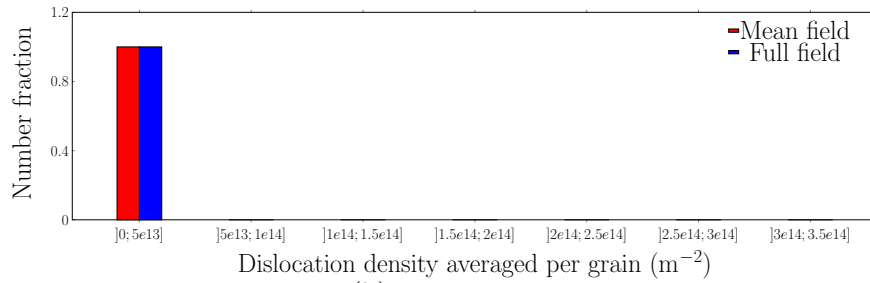


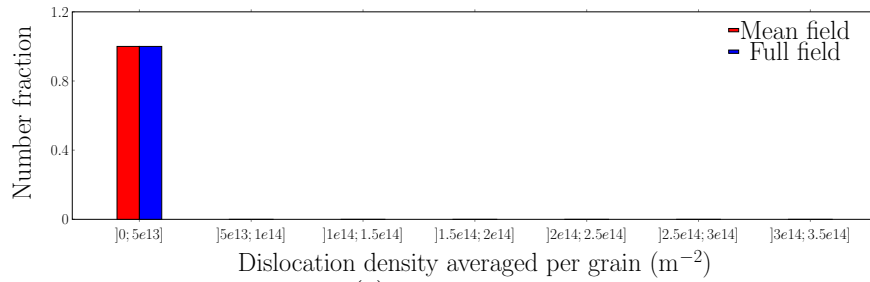
Figure 19: Comparisons, at different instants, of the grain radius distributions ((a) to (d)) obtained during a PDRX process using the present *full field* model and a *mean field* model of the literature [12]. The simulated process is a heat treatment at 1273°K during 25min.



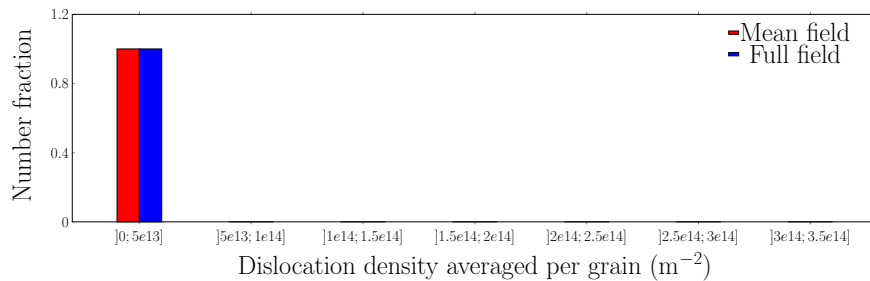
(a) $t = 0\text{min}$



(b) $t = 10\text{min}$



(c) $t = 20\text{min}$



(d) $t = 25\text{min}$

Figure 20: Comparisons, at different instants, of the dislocation density distributions ((a) to (d)) obtained during a PDRX process using the present *full field* model and a *mean field* model of the literature [12]. The simulated process is a heat treatment at 1273°K during 25min.

6. Conclusions

In the present work, a robust 3D model based on the LS method within a FE framework coupled to analytical laws has been presented to model the DRX and PDRX phenomena occurring during and after hot deformation of metals respectively. The advantages of the considered model are large : (i) the model enables to perform 3D simulations; (ii) the mechanisms of strain hardening, static and dynamic recovery are simulated thanks to phenomenological laws coming from a pre-existing *mean field* model [12, 13], which is not as accurate as with a crystal plasticity finite element formulation, but considerably reduces the computational costs of the simulations; (iii) the considered 3D model is able to describe the grain boundary network using the level-set method, even at large deformation (for instance $\varepsilon > 0.2$) in order to reproduce industrial processes and (iv) a sensitivity study has largely minimized computational costs, allowing the integration of the model in an industrial context through the DIGIMU[®] software package.

Results of DRX and PDRX simulations using this new numerical framework were also confronted with the prediction of the above-mentioned *mean field* model [12, 13]. Results have shown that the *mean field* model provides a poor description of the recrystallized fraction and grain size distributions during hot deformation. This difference reinforces the idea that the proposed *full field* model is much more powerful than a *mean field* model since it explicitly takes the grain boundary network into account. After hot deformation, the whole results predicted by the *mean field* model, except the grain size distribution, are close to the *full field* predictions.

Future investigations will aim to (i) improve the *mean field* model by tackling some considered assumptions; (ii) validate the proposed *full field* formalism thanks to experimental results and (iii) confront this model to a crystal plasticity-based DRX *full field* model.

Acknowledgements

The authors thank the AREVA NP, ArcelorMittal, ASCOMETAL, AUBERT & DUVAL, CEA, SAFRAN, TIMET and TRANSVALOR companies and the ANR for

585 their financial support through the DIGIMU consortium and ANR industrial Chair; and Prof. R. Logé for the fruitful discussions concerning the *mean field* model and γ_{NR}/γ_{RX} equations.

Appendices

A. Representation of the grain boundary network

590 The Voronoï method consists in generating a diagram composed of a set of N Voronoï nuclei (S_i). Then, a single Voronoï cells V_i per nucleus is defined following this rule: each Voronoï cell is composed of all points closer to S_i than to any other nuclei. However, the Voronoï method cannot respect a given grain size distribution. Thus, a second method called Laguerre-Voronoï can be used. This method consists in
 595 generating a diagram where the locations of the cells faces are constrained by a given non-intersecting spherical packing. Thus, the diagram is composed of N seeds each with a weight (S_i, r_i) . Then, a single Laguerre-Voronoï L_i is created per seed following this new rule: each Laguerre-Voronoï cell is composed of all points closer to S_i than to any other nuclei, via the power distance. Where the power distance from S_i to x is
 600 defined by $d(x, S_i)^2 - r_i^2$.

B. Level set method for grain boundaries description

A LS function ψ is defined over a domain Ω as the signed distance function to the interface Γ of a sub-domain G of Ω . The values of ψ are calculated at each interpolation point (node in the considered P1 formulation) and the sign convention states $\psi \geq 0$
 605 inside G and $\psi \leq 0$ outside :

$$\begin{cases} \psi(x, t) = \pm d(x, \Gamma), x \in \Omega, \\ \Gamma(t) = \{x \in \Omega, \psi(x, t) = 0\}, \end{cases} \quad (\text{B.1})$$

where d corresponds to the Euclidean distance. The equations to evaluate analytically the LS functions of a Voronoï or a Laguerre-Voronoï tessellation are detailed in [49]. Generally, a single LS function is able to describe a single grain boundary leading to a number of LS functions N equal to the number of grains N_g in the microstructure

610 ($N = N_g$). To limit the number of LS functions and thus the computational cost, a coloring/recoloring technique has recently been developed and applied to this model [31]. This technique aims to gather several grain boundaries in each LS function, leading to a number of LS functions significantly lower than the number of grains ($N \ll N_g$) during all the simulation.

615 C. Grain boundary migration kinetic

To simulate the kinetic of grain boundaries, each LS interface is displaced during the simulation according to a given velocity field \vec{v} by solving a transport equation :

$$\begin{cases} \frac{\partial \psi(x,t)}{\partial t} + \vec{v} \cdot \vec{\nabla} \psi(x,t) = 0, \\ \psi(x,t=0) = \psi^0(x), \end{cases} \quad (\text{C.1})$$

Where $\psi^0(x)$ is the LS interface at $t = 0$ s. The velocity is assumed to be the contribution of two terms :

$$\vec{v} = \vec{v}_c + \vec{v}_e, \quad (\text{C.2})$$

620 where \vec{v}_c and \vec{v}_e are respectively the velocities due to capillarity effects and stored energy gradients expressed as follow :

$$\vec{v}_e = M_b \delta(\dot{\epsilon}) \Delta E \vec{\nabla} \psi, \quad (\text{C.3})$$

$$\vec{v}_c = -M_b \gamma_b \Delta \psi \vec{\nabla} \psi, \quad (\text{C.4})$$

where M_b is the grain boundary mobility, $\delta(\dot{\epsilon})$ is a strain rate dependant parameter detailed in the following, ΔE is the stored energy gradient across the interface and γ_b is the grain boundary energy. These descriptions of the different kinetic terms are correct
625 if the LS function ψ is a distance function (i.e. $\|\nabla \psi\| \equiv 1$) at least inside a thin layer $|\psi| \leq L$ around the interface.

The grain boundary mobility M_b , appearing in Eqs. C.3 and C.4 can be written as a function of temperature :

$$M_b = M_0(T) \exp\left(\frac{-Q_m}{RT}\right), \quad (C.5)$$

630 where Q_m is the activation energy for grain boundary migration, M_0 is the pre-exponential factor and R is the gas constant. In this study, M_b and γ_b are assumed isotropic for all boundaries in the microstructure.

Sometimes, for *mean field* DRX modeling, M_b is a function of strain rate. However, 635 as there is no clear physical explanation for this dependency, and that it seems quite inappropriate to define differently here the mobility for capillarity or stored energy effects, it is preferred to introduce an equivalent formulation where an additional strain rate term (function $\delta(\dot{\epsilon})$) is considered for the definition of velocity due to the stored energy (Eq. C.3). This parameter is defined at different strain rates and a linear inter- 640 polation is made in the model to determine the new value at a given strain rate.

To avoid kinematic incompatibilities and deal with the considered coloring/recoloring scheme, the velocity term \vec{v}_e is evaluated as common for all the LS functions and thanks to the strategy described by Scholtes et al. (sections 3.2, 3.3 and Equation (8) of [32] 645 but where the corresponding mobility M is defined here as $M_b \delta(\dot{\epsilon})$.

Finally, updating the grain boundaries of the whole microstructure is equivalent to solve the convective-diffusive equation of the N LS functions:

$$\begin{cases} \frac{\partial \psi_i(x,t)}{\partial t} - M_b \gamma_b \Delta \psi_i(x,t) + \vec{v}_e \cdot \vec{\nabla} \psi_i(x,t) = 0, \quad \forall i \in \{1, \dots, N\}, \\ \psi_i(x,t=0) = \psi_i^0(x). \end{cases} \quad (C.6)$$

650

The interfaces of every grains belonging to the i^{th} LS function (ψ_i) is thus implicitly given at each time step by the equation $\psi_i(t,x) = 0$. A major drawback of the LS method is the loss of metric properties after the resolution of Eq. C.6. Indeed, even

655 if the LS functions are initialized as distance functions, their metric properties are not
preserved during the resolution of Eq. C.6 and consequently the distance functions
have to be reinitialized after the resolution. In order to reinitialize the metric properties
of the LS functions, a new direct reinitialization method proposed in [58] is used. This
parallel and optimized approach has been proven to be as accurate as a classical direct
660 reinitialization method, while being much faster.

References

- [1] D. Li, Q. Guo, S. Guo, H. Peng, Z. Wu, The microstructure evolution and nucleation mechanisms of dynamic recrystallization in hot-deformed Inconel 625 superalloy, *Materials and Design* 32 (2) (2011) 696–705. doi:10.1016/j.matdes.2010.07.040.
665 URL <http://dx.doi.org/10.1016/j.matdes.2010.07.040>
- [2] H. Jiang, L. Yang, J. Dong, M. Zhang, Z. Yao, The recrystallization model and microstructure prediction of alloy 690 during hot deformation, *Materials and Design* 104 (2016) 162–173. doi:10.1016/j.matdes.2016.05.033.
670 URL <http://dx.doi.org/10.1016/j.matdes.2016.05.033>
- [3] Z. Wan, Y. Sun, L. Hu, H. Yu, Experimental study and numerical simulation of dynamic recrystallization behavior of TiAl-based alloy, *Materials & Design* 122 (2017) 11–20. doi:10.1016/j.matdes.2017.02.088.
URL <http://dx.doi.org/10.1016/j.matdes.2017.02.088>
- 675 [4] K. Huang, R. Logé, A review on dynamic recrystallization phenomena in metallic materials, *Materials & Design* 111 (2016) 548–574. doi:10.1016/j.matdes.2016.09.012.
URL <http://linkinghub.elsevier.com/retrieve/pii/S0264127516311753>
- 680 [5] X. G. Fan, H. Yang, P. F. Gao, R. Zuo, P. H. Lei, The role of dynamic and post dynamic recrystallization on microstructure refinement in primary working of a

- coarse grained two-phase titanium alloy, *Journal of Materials Processing Technology* 234 (2016) 290–299. doi:10.1016/j.jmatprotec.2016.03.031.
URL <http://dx.doi.org/10.1016/j.jmatprotec.2016.03.031>
- 685 [6] M. H. Maghsoudi, A. Zarei-Hanzaki, P. Changizian, A. Marandi, Metadynamic recrystallization behavior of AZ61 magnesium alloy, *Materials and Design* 57 (2014) 487–493. doi:10.1016/j.matdes.2013.12.051.
URL <http://dx.doi.org/10.1016/j.matdes.2013.12.051>
- [7] M. Avrami, Kinetics of Phase Change. I General Theory, *The Journal of Chemical Physics* 7 (12) (1939) 1103–1112. doi:10.1063/1.1750380.
690 URL <http://aip.scitation.org/doi/10.1063/1.1750380>
- [8] M. Avrami, Kinetics of Phase Change. II Transformation Time Relations for Random Distribution of Nuclei, *The Journal of Chemical Physics* 8 (2) (1940) 212–224. doi:10.1063/1.1750631.
695 URL <http://aip.scitation.org/doi/10.1063/1.1750631>
- [9] M. Avrami, Granulation, Phase Change, and Microstructure Kinetics of Phase Change. III, *The Journal of Chemical Physics* 9 (2) (1941) 177–184. doi:10.1063/1.1750872.
URL <http://aip.scitation.org/doi/10.1063/1.1750872>
- 700 [10] F. Montheillet, O. Lurdos, G. Damamme, A grain scale approach for modeling steady-state discontinuous dynamic recrystallization, *Acta Materialia* 57 (5) (2009) 1602–1612. doi:10.1016/j.actamat.2008.11.044.
URL <http://linkinghub.elsevier.com/retrieve/pii/S1359645408008641>
- 705 [11] D. G. Cram, H. S. Zurob, Y. J. M. Brechet, C. R. Hutchinson, Modelling discontinuous dynamic recrystallization using a physically based model for nucleation, *Acta Materialia* 57 (17) (2009) 5218–5228. doi:10.1016/j.actamat.2009.07.024.
URL <http://dx.doi.org/10.1016/j.actamat.2009.07.024>

- 710 [12] P. Bernard, S. Bag, K. Huang, R. Logé, A two-site mean field model of discontinuous dynamic recrystallization, *Materials Science and Engineering: A* 528 (24) (2011) 7357–7367. doi:10.1016/j.msea.2011.06.023.
URL <http://linkinghub.elsevier.com/retrieve/pii/S0921509311006757>
- 715 [13] O. Beltran, K. Huang, R. Logé, A mean field model of dynamic and post-dynamic recrystallization predicting kinetics, grain size and flow stress, *Computational Materials Science* 102 (2015) 293–303. doi:10.1016/j.commatsci.2015.02.043.
URL <http://linkinghub.elsevier.com/retrieve/pii/S0927025615001445>
- 720 [14] L. Maire, B. Scholtes, C. Moussa, N. Bozzolo, D. Pino Muñoz, M. Bernacki, Improvement of 3D mean field models for capillarity-driven grain growth based on full field simulations, *Journal of Materials Science* 51 (24) (2016) 10970–10981. doi:10.1007/s10853-016-0309-6.
725 URL <http://link.springer.com/10.1007/s10853-016-0309-6>
- [15] H. Hallberg, Approaches to Modeling of Recrystallization, *Metals* 1 (1) (2011) 16–48. doi:10.3390/met1010016.
URL <http://www.mdpi.com/2075-4701/1/1/16/>
- [16] A. D. Rollett, D. J. Srolovitz, M. P. Anderson, Simulation and theory of abnormal grain growth-anisotropic grain boundary energies and mobilities, *Acta Metallurgica* 37 (4) (1989) 1227–1240. doi:10.1016/0001-6160(89)90117-X.
730
- [17] A. D. Rollett, D. Raabe, A hybrid model for mesoscopic simulation of recrystallization, *Computational Materials Science* 21 (1) (2001) 69–78. doi:10.1016/S0927-0256(00)00216-0.
735 URL <http://www.sciencedirect.com/science/article/pii/S0927025600002160>
- [18] D. Raabe, Introduction of a scalable three-dimensional cellular automaton with

- a probabilistic switching rule for the discrete mesoscale simulation of recrystallization phenomena, *Philosophical Magazine A* 79 (10) (1999) 2339–2358.
740 doi:10.1080/01418619908214288.
URL <http://www.tandfonline.com/doi/abs/10.1080/01418619908214288>
- [19] D. Raabe, Cellular Automata in Materials Science with Particular Reference to Recrystallization Simulation, *Annual Review of Materials Research* 32 (1)
745 (2002) 53–76. doi:10.1146/annurev.matsci.32.090601.152855.
URL <http://www.annualreviews.org/doi/10.1146/annurev.matsci.32.090601.152855>
- [20] L. Barrales Mora, G. Gottstein, L. Shvindlerman, Three-dimensional grain growth: Analytical approaches and computer simulations, *Acta Materialia* 56 (20)
750 (2008) 5915–5926. doi:10.1016/j.actamat.2008.08.006.
- [21] C. E. Krill, L. Q. Chen, Computer simulation of 3-D grain growth using a phase-field model, *Acta Materialia* 50 (12) (2002) 3059–3075.
doi:10.1016/S1359-6454(02)00084-8.
URL <http://www.sciencedirect.com/science/article/B6TW8-466R5TY-1/2/4e83847503c9ca5646b71d4de608f2fa>
755
- [22] H.-K. Kim, S. G. Kim, W. Dong, I. Steinbach, B.-J. Lee, Phase-field modeling for 3D grain growth based on a grain boundary energy database, *Modelling and Simulation in Materials Science and Engineering* 22 (3) (2014) 034004.
doi:10.1088/0965-0393/22/3/034004.
760 URL <http://stacks.iop.org/0965-0393/22/i=3/a=034004?key=crossref.93bafc2174026807f818a4ef5b7aa405>
- [23] B. Merriman, J. K. Bence, S. J. Osher, Motion of Multiple Junctions: A Level Set Approach, *Journal of Computational Physics* 112 (2) (1994) 334–363.
doi:10.1006/jcph.1994.1105.
765 URL <http://linkinghub.elsevier.com/retrieve/pii/S0021999184711053>

- [24] M. Bernacki, Y. Chastel, T. Coupez, R. Logé, Level set framework for the numerical modelling of primary recrystallization in polycrystalline materials, *Scripta Materialia* 58 (12) (2008) 1129–1132. doi:10.1016/j.scriptamat.2008.02.016.
770 URL <http://linkinghub.elsevier.com/retrieve/pii/S1359646208001425>
- [25] M. Elsey, S. Esedoglu, P. Smereka, Large-scale simulation of normal grain growth via diffusion-generated motion, *Proceedings of the Royal Society A: Mathematical, Physical and Engineering Sciences* 467 (2126) (2011) 381–401. doi:10.1098/rspa.2010.0194.
775
- [26] M. Elsey, S. Esedoglu, P. Smereka, Diffusion generated motion for grain growth in two and three dimensions, *Journal of Computational Physics* 228 (21) (2009) 8015–8033. doi:10.1016/j.jcp.2009.07.020.
780 URL <http://dx.doi.org/10.1016/j.jcp.2009.07.020>
- [27] C. Mießen, M. Liesenjohann, L. Barrales-Mora, L. Shvindlerman, G. Gottstein, An advanced level set approach to grain growth Accounting for grain boundary anisotropy and finite triple junction mobility, *Acta Materialia* 99 (99) (2015) 39–48. doi:10.1016/j.actamat.2015.07.040.
785 URL <http://linkinghub.elsevier.com/retrieve/pii/S135964541500511X>
- [28] R. Logé, M. Bernacki, H. Resk, L. Delannay, H. Dignonnet, Y. Chastel, T. Coupez, Linking plastic deformation to recrystallization in metals using digital microstructures, *Philosophical Magazine* 88 (30-32) (2008) 3691–3712. doi:10.1080/14786430802502575.
790 URL <http://www.tandfonline.com/doi/abs/10.1080/14786430802502575>
- [29] M. Bernacki, R. Logé, T. Coupez, Level set framework for the finite-element modelling of recrystallization and grain growth in polycrystalline materials, *Scripta Materialia* 64 (6) (2011) 525–528. doi:
- 795

10.1016/j.scriptamat.2010.11.032.

URL <http://linkinghub.elsevier.com/retrieve/pii/S1359646210007906>

[30] H. Hallberg, A modified level set approach to 2D modeling of dynamic recrystallization, *Modelling and Simulation in Materials Science and Engineering* 21 (8) (2013) 085012. doi:10.1088/0965-0393/21/8/085012.

URL <http://stacks.iop.org/0965-0393/21/i=8/a=085012?key=crossref.fc2d86d9805f0075a83535b0524735cb>

[31] B. Scholtes, M. Shakoor, A. Settefrati, P.-O. Bouchard, N. Bozzolo, M. Bernacki, New finite element developments for the full field modeling of microstructural evolutions using the level-set method, *Computational Materials Science* 109 (2015) 388–398. doi:10.1016/j.commatsci.2015.07.042.

URL <http://linkinghub.elsevier.com/retrieve/pii/S0927025615004528>

[32] B. Scholtes, R. Boulais-Sinou, A. Settefrati, D. Pino Muñoz, I. Poitault, A. Montouchet, N. Bozzolo, M. Bernacki, 3D level set modeling of static recrystallization considering stored energy fields, *Computational Materials Science* 122 (2016) 57–71. doi:10.1016/j.commatsci.2016.04.045.

URL <http://linkinghub.elsevier.com/retrieve/pii/S0927025616302142>

[33] J. Kroc, Application of Cellular Automata Simulations to Modelling of Dynamic Recrystallization, *Lecture Notes in Computer Science* 2329 (2002) 773–782.

[34] W. Chuan, Y. He, L. H. Wei, Modeling of discontinuous dynamic recrystallization of a near- α titanium alloy IMI834 during isothermal hot compression by combining a cellular automaton model with a crystal plasticity finite element method, *Computational Materials Science* 79 (2013) 944–959. doi:10.1016/j.commatsci.2013.08.004.

URL <http://dx.doi.org/10.1016/j.commatsci.2013.08.004>

- [35] Y. Mellbin, H. Hallberg, M. Ristinmaa, A combined crystal plasticity and graph-based vertex model of dynamic recrystallization at large deformations, *Modelling and Simulation in Materials Science and Engineering* 23 (4) (2015) 045011. doi:10.1088/0965-0393/23/4/045011.
URL <http://www.scopus.com/inward/record.url?eid=2-s2.0-84928999862&partnerID=tZ0tx3y1>
- [36] E. Popova, Y. Staraselski, A. Brahme, R. K. Mishra, K. Inal, Coupled crystal plasticity - Probabilistic cellular automata approach to model dynamic recrystallization in magnesium alloys, *International Journal of Plasticity* 66 (2015) 85–102. doi:10.1016/j.ijplas.2014.04.008.
URL <http://dx.doi.org/10.1016/j.ijplas.2014.04.008>
- [37] P. Zhao, T. Song En Low, Y. Wang, S. R. Niezgoda, An integrated full-field model of concurrent plastic deformation and microstructure evolution: Application to 3D simulation of dynamic recrystallization in polycrystalline copper, *International Journal of Plasticity* 80 (2016) 38–55. arXiv:1509.04953, doi:10.1016/j.ijplas.2015.12.010.
URL <http://dx.doi.org/10.1016/j.ijplas.2015.12.010>
- [38] L. Reyes, P. Páramo, A. Salas Zamarripa, M. de la Garza, M. Guerrero Mata, Grain size modeling of a Ni-base superalloy using cellular automata algorithm, *Materials & Design* 83 (2015) 301–307. doi:10.1016/j.matdes.2015.06.068.
URL <http://linkinghub.elsevier.com/retrieve/pii/S0264127515004189>
- [39] H. Li, X. Sun, H. Yang, A three-dimensional cellular automata-crystal plasticity finite element model for predicting the multiscale interaction among heterogeneous deformation, DRX microstructural evolution and mechanical responses in titanium alloys, *International Journal of Plasticity* 87 (2016) 154–180. doi:10.1016/j.ijplas.2016.09.008.
URL <http://dx.doi.org/10.1016/j.ijplas.2016.09.008>

- [40] M.-S. Chen, W.-Q. Yuan, H.-B. Li, Z.-H. Zou, Modeling and simulation of dynamic recrystallization behaviors of magnesium alloy AZ31B using cellular automaton method, *Computational Materials Science* 136 (2017) 163–172. doi:10.1016/j.commatsci.2017.05.009.
URL <http://linkinghub.elsevier.com/retrieve/pii/S0927025617302392>
- [41] F. Tancret, E. Galindo-Nava, P. E. J. Rivera Díaz-del-Castillo, Dynamic recrystallisation model in precipitation-hardened superalloys as a tool for the joint design of alloys and forming processes, *Materials & Design* 103 (2016) 293–299. doi:10.1016/j.matdes.2016.04.076.
URL <http://linkinghub.elsevier.com/retrieve/pii/S0264127516305561>
- [42] F. Chen, Z. Cui, J. Chen, Prediction of microstructural evolution during hot forging, *Manufacturing Review* 1 (2014) 6. doi:10.1051/mfreview/2014006.
URL <http://mfr.edp-open.org/10.1051/mfreview/2014006>
- [43] Y. Lin, K.-K. Li, H.-B. Li, J. Chen, X.-M. Chen, D.-X. Wen, New constitutive model for high-temperature deformation behavior of inconel 718 superalloy, *Materials & Design* 74 (74) (2015) 108–118. doi:10.1016/j.matdes.2015.03.001.
URL <http://linkinghub.elsevier.com/retrieve/pii/S026130691500076X>
- [44] M. Azarbarmas, M. Aghaie-Khafri, J. M. Cabrera, J. Calvo, Microstructural evolution and constitutive equations of Inconel 718 alloy under quasi-static and quasi-dynamic conditions, *JMADE* 94 (2016) 28–38. doi:10.1016/j.matdes.2015.12.157.
URL http://ac.els-cdn.com/S0264127515310170/1-s2.0-S0264127515310170-main.pdf?{}_tid=8a2afa72-66d4-11e7-abc7-00000aacb35f{&}acdnat=1499845049{&_}5e4ccb87f374a6a8a8030fc2eb25a74c

- [45] D. Weaire, J. P. Kermode, J. Wejchert, On the distribution of cell areas in a Voronoi network, *Philosophical Magazine Part B* 53 (5) (1986) L101–L105. doi:10.1080/13642818608240647.
885 URL <http://www.tandfonline.com/doi/abs/10.1080/13642818608240647>
- [46] Z. Fan, Y. Wu, X. Zhao, Y. Lu, Simulation of polycrystalline structure with Voronoi diagram in Laguerre geometry based on random closed packing of spheres, *Computational Materials Science* 29 (3) (2004) 301–308. doi:10.1016/j.commatsci.2003.10.006.
890 URL <http://linkinghub.elsevier.com/retrieve/pii/S0927025603002209>
- [47] M. Bernacki, H. Resk, T. Coupez, R. E. Logé, Finite element model of primary recrystallization in polycrystalline aggregates using a level set framework, *Modelling and Simulation in Materials Science and Engineering* 17 (6) (2009) 064006. doi:10.1088/0965-0393/17/6/064006.
895 URL <http://stacks.iop.org/0965-0393/17/i=6/a=064006?key=crossref.b10c4b90e783241fcb950f2c83e5932f>
- [48] R. Quey, P. Dawson, F. Barbe, Large-scale 3D random polycrystals for the finite element method: Generation, meshing and remeshing, *Computer Methods in Applied Mechanics and Engineering* 200 (17-20) (2011) 1729–1745. doi:10.1016/j.cma.2011.01.002.
900 URL <http://linkinghub.elsevier.com/retrieve/pii/S004578251100003X>
- [49] K. Hitti, P. Laure, T. Coupez, L. Silva, M. Bernacki, Precise generation of complex statistical Representative Volume Elements (RVEs) in a finite element context, *Computational Materials Science* 61 (2012) 224–238. doi:10.1016/j.commatsci.2012.04.011.
905 URL <http://dx.doi.org/10.1016/j.commatsci.2012.04.011>
- [50] L. Chen, J. Chen, R. A. Lebensohn, Y. Z. Ji, T. W. Heo, S. Bhattacharyya,
910

- K. Chang, S. Mathaudhu, Z. K. Liu, L. Q. Chen, An integrated fast Fourier transform-based phase-field and crystal plasticity approach to model recrystallization of three dimensional polycrystals, *Computer Methods in Applied Mechanics and Engineering* 285 (2015) 829–848. doi:10.1016/j.cma.2014.12.007.
- 915
- [51] U. F. Kocks, Laws for Work-Hardening and Low-Temperature Creep, *Journal of Engineering Materials and Technology* 98 (1) (1976) 76. doi:10.1115/1.3443340.
URL <http://materialstechnology.asmedigitalcollection.asme.org/article.aspx?articleid=1422062>
- 920
- [52] H. Mecking, U. Kocks, Kinetics of flow and strain-hardening, *Acta Metallurgica* 29 (11) (1981) 1865–1875. doi:10.1016/0001-6160(81)90112-7.
- [53] A. Yoshie, H. Morikawa, Y. Onoe, K. Itoh, Formulation of static recrystallization of austenite in hot rolling process of steel plate., *Transactions of the Iron and Steel Institute of Japan* 27 (6) (1987) 425–431. doi:10.2355/isijinternational1966.27.425.
URL <http://joi.jlc.jst.go.jp/JST.Journalarchive/isijinternational1966/27.425?from=CrossRef>
- 925
- [54] F. J. Humphreys, M. Hatherly, *Recrystallization and related annealing phenomena*, Elsevier, 2004.
- 930
- [55] J. E. Bailey, P. B. Hirsch, The Recrystallization Process in Some Polycrystalline Metals, *Proceedings of the Royal Society A: Mathematical, Physical and Engineering Sciences* 267 (1328) (1962) 11–30. doi:10.1098/rspa.1962.0080.
URL <http://rspa.royalsocietypublishing.org/cgi/doi/10.1098/rspa.1962.0080>
- 935
- [56] P. Peczak, M. J. Luton, The effect of nucleation models on dynamic recrystallization I. Homogeneous stored energy distribution, *Philosophical Magazine Part B* 68 (1) (1993) 115–144. doi:10.1080/13642819308215285.

URL <http://www.tandfonline.com/doi/abs/10.1080/13642819308215285>

940

[57] K. Huang, Towards the modelling of recrystallization phenomena in multi-pass conditions: application to 304L steel, Ph.D. thesis (2012).

URL <https://pastel.archives-ouvertes.fr/pastel-00682138>

[58] M. Shakoar, B. Scholtes, P.-O. Bouchard, M. Bernacki, An efficient and parallel level set reinitialization method Application to micromechanics and microstructural evolutions, *Applied Mathematical Modelling* 39 (23-24) (2015) 7291–7302. doi:10.1016/j.apm.2015.03.014.

945

URL <http://linkinghub.elsevier.com/retrieve/pii/S0307904X15001638>